FINAL TECHNICAL REPORT

Unraveling the Role of Transport, Electrocatalysis, and Surface Science in the Solid Oxide Fuel Cell Cathode Oxygen Reduction Reaction

Project Number: FE0009656

Submitted by
Srikanth Gopalan
Department of Mechanical Engineering &
Division of Materials Science and Engineering
Boston University
Boston, MA 02215

Disclaimer

TABLE OF CONTENTS

ABSTRACT

This final report for project FE0009656 covers the period from 10/01/2012 to 09/30/2015 and covers research accomplishments on the effects of carbon dioxide on the surface composition and structure of cathode materials for solid oxide fuel cells (SOFCs), specifically $La_{1-x}Sr_xFe_yCo_{1-y}O_{3-\delta}$ (LSCF). Epitaxially deposited thin films of LSCF on various single-crystal substrates have revealed the selective segregation of strontium to the surface thereby resulting in a surface enrichment of strontium. The near surface compositional profile in the films have been measured using total x-ray fluorescence (TXRF), and show that the kinetics of strontium segregation are higher at higher partial pressures of carbon dioxide. Once the strontium segregates to the surface, it leads to the formation of precipitates of SrO which convert to $SrCO_3$ in the presence of even modest concentrations of carbon dioxide in the atmosphere. This has important implications for the performance of SOFCs which is discussed in this report. These experimental observations have also been verified by Density Functional Theory calculations (DFT) which predict the conditions under which SrO and $SrCO_3$ can occur in LSCF. Furthermore, a few cathode compositions which have received attention in the literature as alternatives to LSCF cathodes have been studied in this work and shown to be thermodynamically unstable under the operating conditions of the SOFCs.

EXECUTIVE SUMMARY

This final report for project FE0009656 covers the period from 10/01/2012 to 09/30/2015 and covers research accomplishments on the effects of carbon dioxide on the surface composition and structure of cathode materials for solid oxide fuel cells (SOFCs), specifically $La_{1-x}Sr_xFe_yCo_{1-y}O_{3-\delta}$ (LSCF). Much of the detailed research results stemming from this work have been presented in periodic quarterly technical reports. Thus, the purpose of this final technical report is to provide a summary of the most important results and its implications for the operation of SOFCs.

In the first part of the report, we focus on experiments conducted at the NSLS light source at Brookhaven National Laboratory. These experiments were conducted on high quality model thin films of LSCF deposited on various single crystal substrates using pulsed laser deposition (PLD). After annealing the films in cathodic atmosphere of interest, the near surface compositional profiles in the films were measured using total x-ray fluorescence (TXRF) which revealed clear evidence of strontium segregation to the LSCF film surface. Further exploration of the film surfaces using hard x-ray photoelectron spectroscopy (HAXPES) revealed evidence of Sr-O and Sr-CO_3 coordination in the near surface region, strongly implying the formation of SrO and $SrCO_3$ phases. Separate studies of the surface region of the films using atomic force microscopy (AFM) also revealed the existence of second phase precipitates covering the surface. These studies are also coupled with Density Functional Theory (DFT) calculations which confirm that the formation of SrO and $SrCO_3$ from LSCF can occur under certain conditions of temperature, oxygen partial pressure, and carbon dioxide partial pressure. Coupled with these studies, DFT studies have also been used to probe the surface structure of LSCF. Specifically, the oxygen vacancy concentrations in the bulk and near surface regions of LSCF have been computed using DFT.

In the second part of the report, we report on cathode materials which have recently been proposed as alternates to LSCF due to their high performance. We show using an equilibration technique known as the molten salt method, that a few of the proposed materials are unstable under the operating conditions of the SOFCs.

PROJECT DETAILS

Task 1: Project Management, Planning and Reporting

Under this task, weekly meetings were held. During these meetings, we discussed the work conducted in the preceding week, set future direction, and discussed manuscripts in progress. Reports to DOE were submitted as required.

Task 2: Fabrication of micropatterned thin films and heteroepitaxial thin films

Due to the realignment of priorities at Pacific Northwest National Lab's Environmental Molecular Sciences (EMSL) lab, we decided to change focus from the micropatterned thin film samples and the ensuing tasks and instead focus our attention on surface spectroscopy measurements, cathode stability, segregation effects. Thus, only heteroepitaxial thin films were fabricated under this task. About 25 samples of LSCF were fabricated on various single crystal substrates. These thin film heteroepitaxial samples were used in a variety of other tasks.

Task 3: AC Impedance spectroscopy on patterned films

Since micropatterning services were unavailable, effort in this task and task 4 were suspended and reassigned to other tasks.

Task 4: Transport multiphysics modeling

See above.

Task 5: X-Ray spectroscopy

Total reflection x-ray fluorescence (TXRF) and hard x-ray photoelectron spectroscopy (HAXPES) are the principal tools used to characterize the films obtained in task 2. These studies have clearly revealed the conditions and extent of strontium segregation and carbonate formation.

Task 6: TEM, SEM, and AFM studies

Transmission electron microscopy (TEM), scanning electron microscopy (SEM) and atomic force microscopy (AFM) techniques have been utilized to characterize heteroepitaxial films to judge film quality and lattice match.

We describe the results obtained from tasks 5 and 6 in the attached manuscript. An abstract describing the results is provided below followed by a bulleted list of accomplishments. Complete details can be found in the manuscript.

Effect of atmospheric CO_2 on surface segregation and phase formation in $La_{0.6}Sr_{0.4}Co_{0.2}Fe_{0.8}O_{3-\delta}$ thin films (Manuscript Attached)

Abstract: In this paper, we describe the effects of atmospheric CO_2 on surface segregation and phase formation in $La_{0.6}Sr_{0.4}Co_{0.2}Fe_{0.8}O_{3-\delta}$ (LSCF-6428). (0 0 1)-oriented LSCF-6428 thin films

were deposited on lattice matched (1 1 0)-oriented $NdGaO_3$ (NGO) substrates by pulsed laser deposition (PLD). Using the synchrotron technique of total reflection X-ray fluorescence (TXRF), it was found that the kinetics of Sr-surface segregation was enhanced when annealing at 800◦C in a high-CO2partial pressure, as compared to a similar anneal in a CO_2-free atmosphere, with the oxygen partial pressure being constant in both cases. Hard X-ray photo-electron spectroscopy (HAXPES) measurements showed that the contribution of the surface carbonate to surface oxide phases increased significantly for the sample annealed in the high-CO_2 atmosphere. Atomic force microscopy (AFM) studies showed enhanced surface phase formation during the high-CO_2 partial pressure anneal. Density functional theory (DFT) calculations provide a thermodynamic basis for the enhanced kinetics of surface segregation in the presence of atmospheric CO_2.

Key accomplishments described in the paper:

1) Measurement of extent of Sr-segregation in LSCF.
2) Obtaining evidence of surface precipitation of SrO and $SrCO_3$ on LSCF surfaces which have implications for cathode performance.
3) Computational validation of experimentally observed Sr-segregation using DFT.

Task 7: Effect of CO2 Impurity

Several alternate cathode compositions were studied as part of this study to obtain high performance cathodes. In particular, we studied the stability of $Ba_{0.5}Sr_{0.5}Co_{0.8}Fe_{0.2}O_{3-\delta}$ (BSCF), $Sr_2Fe_{1.5}Mo_{0.5}O_{6-\delta}$ (SFM) and $La_{0.6}Sr_{0.4}Co_{0.2}Fe_{0.8}O_{3-\delta}$ (LSCF). The first two of these materials BSCF and SFM have been proposed as high performance alternate cathode materials to LSCF. Our studies have revealed that neither BSCF nor SFM are stable under cathodic conditions in air, whereas LSCF is stable. An abstract of the results is provided below followed by a list of accomplishments. More details can be found in the attached manuscript with a list of implications for SOFC performance.

Thermodynamic stabilities of $Ba_{0.5}Sr_{0.5}Co_{0.8}Fe_{0.2}O_{3-\delta}$, $Sr_2Fe_{1.5}Mo_{0.5}O_{6-\delta}$ and $La_{0.6}Sr_{0.4}Co_{0.2}Fe_{0.8}O_{3-\delta}$ using molten salt method (Manuscript Attached)

Abstract: $Ba_{0.5}Sr_{0.5}Co_{0.8}Fe_{0.2}O_{3-\delta}$ (BSCF), $Sr_2Fe_{1.5}Mo_{0.5}O_{6-\delta}$ (SFM) and $La_{0.6}Sr_{0.4}Co_{0.2}Fe_{0.8}O_{3-\delta}$ (LSCF) are three, promising cathode materials for application in low temperature SOFC systems. In this work, their stability has been tested by equilibrating them in a eutectic molten salt mixture of LiCl-KCl in air. Both single-phase BSCF and SFM decomposed into their carbonate and oxide precursors in air, but LSCF retained its single phase. This study suggests that BSCF and SFM cathode materials are thermodynamically unstable with respect to their carbonate precursors in eutectic molten salts in air.

Key accomplishments described in the paper:

1) BSCF and SFM two recent materials that have been suggested as high performance SOFC cathode materials have been found to be unstable in the operating conditions of the SOFCs and are thus deemed unsuitable from the standpoint of long term performance.
2) LSCF on the other hand remains stable under the same conditions.

Implications for SOFC performance

The implications of these results for SOFCs are very clear. These results clearly preclude the use of BSCF and SFM as SOFC cathodes since they decompose to the alkaline earth carbonates even in air. Thus, even though BSCF and SFM may possess excellent oxygen surface exchange kinetics, and are excellent MIECs, their instability with respect to decomposition into alkaline earth carbonates makes them unsuitable for application as SOFC cathodes.

Task 8: Defect Modeling and Task 9: Quantum mechanical modeling of cathodes and cathode - gas interfaces

Under these tasks point defects in cathode materials have been modeled using a combination of classical thermodynamics. The concentrations of the point defects have been computed as a function of temperature and oxygen partial pressure and their role in the stability of LSCF towards reaction with carbon dioxide have been explored using density functional theory (DFT). The results are described in the abstract of a published manuscript below followed by key accomplishments and implications for SOFC operation. More details can be found in the manuscript.

Predicting oxygen vacancy non-stoichiometric concentration in perovskites from first principles (Manuscript Attached)

Abstract: Formation of oxygen vacancies by introducing various mixed-valent cation dopants is a common practice to improve the cathode performance in solid oxide fuel cells. A computational procedure is developed in this work to predict the equilibrium oxygen vacancy non-stoichiometric concentrations at experimentally relevant temperatures and oxygen partial pressures for both bulk and surface oxide phases. The calculations are based on the first-principles density functional theory and a constrained free-energy functional. Quantitative agreements are found by direct comparisons to the thermogravimetry and solid electrolyte coulometry measurements for the strontium-doped lanthanum cobalt iron oxides at different compositions. Our results indicate that the oxygen vacancies are energetically stabilized at surfaces for all temperatures and all oxygen partial pressures, while such surface stabilization effects become stronger at higher temperatures and lower oxygen partial pressures.

Key accomplishments described in the paper:

1) A computational methodology to compute the equilibrium oxygen vacancies in the bulk and the surface regions has been developed.

Implications of surface chemistry measurements and computations for SOFC performance

The results of our x-ray spectroscopic measurements and our DFT computations in the present project clearly demonstrate the segregation of Sr to the LSCF surface and the formation of SrO which subsequently transforms to $SrCO_3$ in the presence of even trace amounts of CO_2 always present in ambient air. It is therefore possible that pore surfaces of LSCF in service as SOFC cathodes are always coated with a layer of $SrCO_3$. So long as the stack is operated in air as the oxidant, a small surface layer of $SrCO_3$ is not expected to be deleterious to cell operation.

However, if there is a significant leak of depleted anode gas into the cathodic chamber either through pin-holes in the electrolyte or through back diffusion (as is possible in some stack designs), large amounts of surface $SrCO_3$ formation is assured and this could have a deleterious effect on the combined surface adsorption, diffusion and eventual electronation of oxygen, especially at lower temperatures. In prior work on patterned LSCF electrodes, we found that the ratio of the surface diffusion to bulk diffusion in LSCF decreased with decreasing temperature at fixed oxygen partial pressure. This is anomalous since the oxygen vacancy concentration is expected to decrease with decreasing temperature at a fixed oxygen partial pressure, thereby favoring surface diffusion over bulk diffusion. At the time we obtained these results, we were unable to explain this anomalous observation. The present spectroscopy measurements, combined with DFT computations provide a likely explanation. At lower temperatures, the formation of the Sr-rich surface phases such as SrO and $SrCO_3$, likely inhibit surface diffusion, thereby rendering bulk diffusion a relatively more facile diffusion pathway. Thus, the conventional expectation that bulk diffusion pathways are always dominant in an MIEC such as LSCF may not always be hold true, especially when large concentrations of carbon dioxide enter the cathodic gas stream leading to formation of Sr-rich surface phases.

While the short term impacts of Sr segregation phenomena are clear, longer term test data on field-tested cells and stacks are required to make further inroads into understanding the impact of Sr-segregation and the formation of surface phases.

Task 10: Fabrication and testing of single cells and comparison to baseline data and Task 11: Polarization Loss Modeling

As seen from task 7, our alternate cathode materials turned out to be unstable. Thus effort under these tasks were refocused on tasks 5, 6, 8, and 9. Future work will focus on finding stable high performance cathode materials.

CONCLUSIONS AND SUMMARY

Our spectroscopy, TEM, and AFM results combined with our DFT defect modeling clearly show the driving forces for Sr-segregation and the conditions under which strontium oxide and strontium carbonate formation are expected to occur. In particular our work clearly demonstrates surface formation of $SrCO_3$ under SOFC operating conditions. However, this surface formation of $SrCO_3$ under normal operating conditions is not expected to be deleterious to SOFC performance. By contrast, if large concentrations of carbon dioxide leaked into the air chamber significant formation of $SrCO_3$ is expected which could have a deleterious effect on SOFC performance.

Our present study has also clearly demonstrated the instability of BSCF and SFM cathodes in air and the stability of LSCF cathodes. Thus LSCF is likely to be the leading choice for SOFC cathodes until other high performance cathodes which are also stable under SOFC operating conditions are found.

MILESTONE LOG

Milestone (Year 1)	Completion Date	Verification
1) Finalizing process conditions for deposition of at least two heteroepitaxial thin films of new cathode materials on lattice matched substrates beyond baseline LSM and LSCF	Completed 12 months	SEM, TEM of deposited films
2)Finalizing process conditions for deposition ofat least two new micropatterned polycrystalline cathode materials and corresponding electrocatalysts.	We have changed to porous electrodes for these experiments Completed 12 months	SEM of porous electrode films.
3) Screen materials using DFT and patterned electrode cells and make one preliminary recommendation for full cell fabrication and testing	DFT calculations of LSCF complete. Completed at 33 months	Predictions compared against experiment. However, alternate cathode materials proposed turned out to be unstable.
4) Make and test at least one baseline (LSM cathode) cell and one cell with new materials set; Demonstrate at least 20% performance improvement	Combined with milestone 6.	
Milestone (Year 2)	**Completion Date**	**Verification Method**
5) Complete screening using DFT and patterned electrode and make final recommendations for cell making	DFT calculations completed by 33 months.	Predictions compared against experiment

6) Demonstrate 50% improvement in performance over baseline and stability that shows 0.1% or less degradation in cell performance.	Not demonstrated due to thermodynamic instability of proposed alternate cathode materials.	Verified that proposed alternate cathode materials are unstable under cathodic conditions.
7) Finalize cell making process conditions and make recommendations to DOE	Not demonstrated due to instability of proposed alternate cathode materials.	Verified that proposed alternate cathode materials are unstable under cathodic conditions.
8) Submit final report to DOE	Will be completed in the extension year 3. Month 36. Milestone number changed to #10	Submission of report to DOE
Milestone (Year 3)	**Completion Date**	**Verification Method**
5) Complete screening using DFT and patterned electrode and make final recommendations for cell making	DFT calculations completed by 33 months. Alternate materials not demonstrated due to thermodynamic instability.	Predictions compared against experiment. Alternate materials not demonstrated due to thermodynamic instability.
6) Demonstrate 50 % improvement in performance over baseline and stability that shows 0.1% or less degradation in cell performance.	Not demonstrated due to instability of proposed alternate cathode materials.	Verified that proposed alternate cathode materials are unstable under cathodic conditions.

7) Finalize cell making process conditions and make recommendations to DOE	Not demonstrated due to instability of proposed alternate cathode materials.	Verified that proposed alternate cathode materials are unstable under cathodic conditions.
8) Determine effect of carbon dioixde on cathode surface chemistry.	Completed month 36. Surface segregation effects of Sr clearly demonstrated.	Through spectroscopic techniques
9) Determine effect of cathode side carbon dioxide on cell performance	Completed month 33. Demonstrated thermodynamic instability of alternate cathode materials in air. Demonstrated stability of LSCF in air.	Molten salt experiment and x-ray diffraction.
10) Submit final report to DOE	Month 36	Submission of final report to DOE

Effect of Atmospheric CO_2 on Surface Segregation and Phase Formation in $La_{0.6}Sr_{0.4}Co_{0.2}Fe_{0.8}O_{3-\delta}$ Thin Films

Yang Yu[a], Heng Luo[b], Deniz Cetin[a], Xi Lin[a,b], Karl Ludwig[a,c], Uday Pal[a,b] Srikanth Gopalan[a,b] and Soumendra Basu[a,b,*]

[a]Division of Materials Science and Engineering, Boston University, Brookline, MA 02446, USA
[b]Department of Mechanical Engineering, Boston University, Boston, MA 02215, USA
[c]Department of Physics, Boston University, Boston, MA 02215, USA

Abstract

The effects of atmospheric CO_2 on surface segregation and phase formation in $La_{0.6}Sr_{0.4}Co_{0.2}Fe_{0.8}O_{3-\delta}$ (LSCF-6428) were investigated. (001)-oriented LSCF-6428 thin films were deposited on lattice matched (110)-oriented $NdGaO_3$ (NGO) substrates by Pulsed Laser Deposition (PLD). Using the synchrotron technique of Total Reflection X-ray Fluorescence (TXRF), it was found that the kinetics of Sr surface segregation was enhanced when annealing at 800°C in a high CO_2 partial pressure, as compared to a similar anneal in a CO_2-free atmosphere, with the oxygen partial pressure being constant in both cases. HArd X-ray PhotoElectron Spectroscopy (HAXPES) measurements showed that the contribution of the surface carbonate to surface oxide phases increased significantly for the sample annealed in the high-CO_2 atmosphere. Atomic Force Microscopy (AFM) studies showed enhanced surface phase formation during the high-CO_2 partial pressure anneal. Density functional theory (DFT) calculations provide a thermodynamic basis for the enhanced kinetics of surface segregation in the presence of atmospheric CO_2.

* Corresponding Author: Soumendra Basu, basu@bu.edu, 1-617-353-6728

Keywords: solid oxide fuel cells, cathode material, lanthanum strontium cobalt iron oxide, CO_2 effect, Sr surface segregation, phase formation

1. Introduction

40% strontium doped lanthanum cobalt iron oxide, $La_{0.6}Sr_{0.4}Co_{0.2}Fe_{0.8}O_{3-\delta}$ (LSCF-6428), is a commonly used perovskite-type material for cathodes in solid oxide fuel cells (SOFCs). The advantages of LSCF-6428 lie in its mixed ionic and electronic conductor (MIEC) behavior and its excellent thermal expansion coefficient (TEC) match with the electrolyte, which is often yttria stabilized zirconia (YSZ) and gadolinium doped ceria (GDC) [1]. In spite of these advantages, when operated at working temperature of SOFCs (typically, >800°C), LSCF-6428 suffers from long-term stability issues [2-5]. This has negative implications for long-term usage of these cathode materials.

Strontium segregation to the surface of LSCF-6428 during annealing at elevated temperatures in the form of strontium oxide (SrO) and strontium carbonate ($SrCO_3$) has been reported previously [6, 7]. Oh et al. reported that the formation of Sr-rich precipitates was enhanced with increasing temperature and oxygen partial pressure [6]. Davis et al. reported $SrCO_3$ formation on LSCF-6428 thin films after annealing at 800°C in air, using hard x-ray photoelectron spectroscopy (HAXPES) [7]. The formation of $SrCO_3$ was attributed to the presence of CO_2 in the atmosphere. It was speculated that SrO is formed at the surface due to Sr surface segregation, leading to the formation of SrO by reaction with atmospheric oxygen. Reaction of SrO with atmospheric CO_2 leads to the formation of $SrCO_3$. It is also possible that CO_2 will directly react with the enhanced Sr concentration at the surface of LSCF-6428 in the presence of O_2 to form SrO and $SrCO_3$. The formation of these surface phases will be deleterious to the electrochemical performance of the device not only because SrO and $SrCO_3$ are both electrical insulators, but also because formation of these surface phases reduces the effective LSCF-6428 surface area for oxygen incorporation, which is an important step in oxygen reduction reaction (ORR) process. The anode exhaust gas in SOFCs undergoing an anode gas recycle process can contain as much as 30% CO_2 produced by hydrocarbon fuels [8]. Any gas leakage from the anode side resulting from crack formation in the seals, electrolyte or interconnects will risk exposing the cathode to this high CO_2

concentration. For this reason, a 30% CO_2 gas phase concentration is chosen as the high-CO_2 concentration in this study.

Different CO_2 partial pressures were applied for real-time TXRF studies at typical SOFC working temperature 800°C, aiming to probe the kinetics of Sr segregation at the surface of LSCF-6428 thin films. AFM studies were performed to examine morphological changes on the surface and DFT calculations were used to explain the mechanism of the segregation.

2. Material and Methods

In this study, LSCF-6428 thin films were grown epitaxially on single crystal lattice matched substrates to get a smooth surface/gas interface suited for grazing incident angle x-ray studies. Epitaxial LSCF-6428 thin films were deposited on lattice matched 10×10×0.5 mm^3 single crystal (110) $NdGaO_3$ (NGO, CrysTec) substrates by pulsed laser deposition (PLD) at the Environmental Molecular Sciences Laboratory (EMSL) at Pacific Northwestern National Laboratory (PNNL). The films were deposited using a LSCF 6428 target, at an oxygen partial pressure of 10 mTorr, and with the substrate heated to 550°C. The heteroepitaxy of (001) LSCF-6428 || (110) NGO was confirmed by x-ray diffraction (XRD) analysis (Figure 1a). Figure 1b shows a cross-section of a focused ion beam (FIB) assisted cross-section of the thin film, showing that the heteroepitaxial film was ~ 250 nm in thickness.

Real-time total reflection x-ray fluorescence (TXRF) measurements were carried out at the X23A2 beamline at the National Synchrotron Light Source-I (NSLS-I) at Brookhaven National Laboratory (BNL). TXRF is a non-destructive method to probe the surface composition of materials. The technique does not require ultra-high vacuum, and thus allows *in-situ* high temperature studies of samples exposed to different atmospheres. The X23A2 beamline is equipped with a Vortex four-element detector with a resolution of approximately 220eV at 6keV [9]. In these experiments, each of the four elements in LSCF was first 'windowed' by capturing their corresponding fluorescence peaks summed by four single channel analyzers (SCA). The data was then input into a multiple channel analyzer (MCA). The materials used to 'window' each element were a $LaAlO_3$ target for La, a $SrTiO_3$ target for Sr, a Co_2O_3 sheet for Co, and a

Fe_2O_3 sheet for Fe. The fluorescence lines used for window each element were $L\alpha_1$ for La, and $K\alpha_1$ for Sr, Fe, and Co.

Figure 2 shows the schematic of the TXRF setup. A specially designed stainless steel chamber was used that allows incoming and outgoing x-ray beams as well as the fluorescence signals from the sample to go through its Kapton window. The x-ray fluorescence signals are collected using a fluorescence detector facing the Kapton window of the chamber. The chamber is capable of heating a sample up to 1000°C with flowing gases. This chamber was fixed onto a Huber goniometer that can tilt the sample relative to the beam during the experiments.

Before taking measurements, the chamber was first flushed with the desired gas composition with a volume 15 times larger than the chamber volume to ensure that all residual gases in the chamber are removed. The gas compositions for the two experiments were 30% CO_2 - 21% O_2 - 49% N_2 for the 'high CO_2' concentration experiments and 21% O_2 - 79% N_2 for the 'CO_2-free' experiments. In both cases, the oxygen partial pressure was 0.21 atm. After the environment achieved desired gas phase composition, the sample was heated to 800°C in 40 minutes. The chamber was then kept heated at 800°C for 9 hours. Scanning the incoming x-ray over a range of incidence angles starting with a grazing angle and collecting the fluorescence signals for all the elements carried out depth profiling of all the elements. Each such scan lasted for ~ 45 minutes. At large incident angles, the x-ray beam penetrates deep into the sample and the detector gets signals from the substrate as well as from the thin film. As the incident angle is reduced, the depth from which the signal is collected reduces. Below a certain angle, known as the critical angle θ_c, the x-ray beam is totally reflected and only the topmost ~10 nanometers of the thin film fluoresces giving the surface composition of the film.

After the real-time TXRF measurements, the samples were cooled down to room temperature. Atomic force microscopy studies were carried out on the post-annealed samples using a Bruker Dimension 3000 AFM.

Hard x-ray photoelectron spectroscopy (HAXPES) measurements on the post-annealed TXRF samples were carried out in Beamline X24A at the NSLS. Incident photon energy of 2140 eV was used, and the energy was calibrated using the 3d binding energy of silver (Ag $3d_{5/2}$=368.27 eV) measured from a silver foil. The strontium 3d peak is a doublet from spin orbit splitting into

$3d_{3/2}$ and $3d_{5/2}$. Curve fitting was carried out in the same manner as reported by van der Heide [4]. To distinguish between surface phases, Sr $3d_{5/2}$ peaks corresponding to 133.0 and 134.0 eV energies, were attributed to surface strontium oxide (SrO) and surface strontium carbonate ($SrCO_3$), respectively [4].

3. Results

In the TXRF experiment, the incoming photon energy was set above the Sr K-edge. Figure 3 shows a typical raw data set of photon counts versus incident angle for Sr and La. The photon intensity of the i^{th} component, $I_i(\gamma)$, is a function of the incident angle γ, and is proportional to the concentration of the i^{th} component in the material, $N_i(\gamma)$:

$$N_i(\gamma) \propto I_i(\gamma) \quad [1]$$

Defining the proportionality constants for Sr and La as α and β, gives:

$$N_{Sr} = \alpha \cdot I_{Sr} \quad [2]$$

$$N_{La} = \beta \cdot I_{La} \quad [3]$$

At any x-ray incident angle, the A-site Sr concentration, $R_{Sr/(Sr+La)}$, can then be represented by measured intensities I_{Sr} and I_{La} as:

$$R_{Sr/(Sr+La)} = \frac{N_{Sr}}{N_{Sr} + N_{La}} = \frac{I_{Sr}}{I_{Sr} + C \cdot I_{La}}, \quad [4]$$

where C is a constant defined as:

$$C = \frac{\beta}{\alpha} \quad [5]$$

The constant C can now be expressed in terms of the measured intensities, I_{Sr} and I_{La}, and $R_{Sr/(Sr+La)}$ as:

$$C = \frac{I_{Sr}(1 - R_{Sr/(Sr+La)})}{R_{Sr/(Sr+La)} I_{La}} \quad [6]$$

We know that for LSCF-6428, $R_{Sr/(Sr+La)} = 0.4$ in the bulk. With increasing incident angle of x-ray beam the La and Sr signals asymptotically reach the bulk value (Figure 3) as the surface contribution gets to be vanishingly small with increasing depth from which information is collected. Using these bulk intensities, and the value of $R_{Sr/(Sr+La)}$ in the bulk, C can be calculated using Eq. 6. Knowing C and the measured intensities, I_{Sr} and I_{La}, $R_{Sr/(Sr+La)}$ can then be plotted for all angles using Eq. 4.

Processed data for the *in-situ* TXRF measurements for LSCF-6428 thin films at 800°C are plotted as $R_{Sr/(Sr+La)}$ versus the incident angle of the x-ray beam. Figures 4a and 4b show the results for the 'high CO_2' and 'CO_2-free' cases, respectively. The total high-temperature exposure time in both experiments was ~ 9 hours. Since information on surface segregation is present in the data collected at incident angles below the critical angle, data is presented only for incident angles close to the θ_c.

Figure 5 shows the Sr 3d peaks measured by HAXPES, for an as-deposited sample, as well as the post-annealed samples in CO_2-free and high CO_2 atmospheres. The peaks have been fit to three separate $3d_{3/2}$ and $3d_{5/2}$ doublets, corresponding to surface SrO, surface $SrCO_3$ and bulk perovskite phases. The figure shows that while there is some surface phases form in the as-deposited sample, the high temperature exposures clearly lead to enhanced surface phase formation. The figure also shows that the surface carbonate to surface oxide contributions is much more enhanced for the high-CO_2 case.

4. Discussion

The critical angle, θ_c, for LSCF-6428 at 800°C for an incident x-ray beam with energy of 16.3 keV is calculated to be 0.17 degrees. To understand surface segregation, it is best to start at the dashed line in Figure 4 that marks the critical angle and look at the trends going towards lower

angles to the left. This gives the profile of Sr/(Sr+La) ratio going from the bulk towards the surface of the thin film.

It is interesting to note in Figure 4 that the as-deposited film is actually Sr-poor (La-rich) at the surface. However, in both cases, Sr segregation to the surface of the LSCF-6428 thin films occurs on annealing, with the amount of Sr segregation increasing with annealing time at 800°C (Figures 4a and 4b). In both cases, by the end of the anneal, the surface Sr enhancement exceeds the bulk value of 0.4, in spite of the original as-deposited surface being Sr-poor. In the high-CO_2 atmosphere, the Sr surface segregation appears to reach a stable value after 2 hours of annealing, and does not change appreciably during the subsequent annealing time. In contrast, for the CO_2-free case, Sr continues to segregate to the surface even after 9 hours of annealing. This is a clear indication that the kinetics of Sr surface segregation is enhanced in high-CO_2 case. It should be mentioned that no changes were observed on the B-site cation sublattice and the ratio of Co to Fe signals remain unchanged during annealing.

For the formation of surface $SrCO_3$ in the high CO_2 case, two possible mechanisms are proposed. The first can be pictured as a two-step process. The first step is the formation of a surface SrO phase by the reaction of enriched surface Sr with atmospheric oxygen (Eq. 7). This is followed by the formation of a surface $SrCO_3$ phase by reaction of the SrO with atmospheric CO_2 (Eq. 8).

$$Sr + \frac{1}{2}O_2(g) \Leftrightarrow SrO \qquad [7]$$

$$SrO + CO_2 \Leftrightarrow SrCO_3 \qquad [8]$$

At 800°C, the equilibrium CO_2 partial pressure for $SrCO_3$ formation (by Eq. 8) is 1.7×10^{-3} atm [7]. Since the high-CO_2 partial pressure of 0.3 atm is well above the equilibrium value, the formation of $SrCO_3$ is thermodynamically favored. The formation of $SrCO_3$ removes the reactant, SrO in the second step (Eq. 8), which is also the product in the first step (Eq. 7). By removing the product, the kinetics of Sr surface segregation in step 1 is enhanced.

The second mechanism does not require an initial formation of SrO to form $SrCO_3$, provided of course that the gas-phase CO_2 partial pressure is high enough. In this case, the Sr in the lattice reacts with gas phase O_2 and CO_2 to form $SrCO_3$ directly (Eq. 9).

$$La_{0.75}Sr_{0.25}Co_{0.25}Fe_{0.75}O_{3-\delta} + \frac{1}{16}O_2 + \frac{1}{8}CO_2 \Leftrightarrow La_{0.75}Sr_{0.125}Co_{0.25}Fe_{0.75}O_{3-\delta} + \frac{1}{8}SrCO_3 \qquad [9]$$

The composition of the LSCF is chosen to be different from LSCF-6428 to reduce the number of unit cells required for the composition and hence reduce computation time for the density functional theory (DFT) calculations. However, it is believed that the trends are still valid for the LSCF-6428 case. The DFT calculations performed here pertain to calculating Gibbs free energy changes for the overall reaction given in Equation 9 and are independent of the mechanistic details of $SrCO_3$ formation. One could potentially conceive of separating the overall reaction given in Equation 9 into two sub-steps, one involving the formation of SrO from $La_{0.75}Sr_{0.25}Co_{0.25}Fe_{0.75}O_3$, and a second involving formation of $SrCO_3$ from SrO through Equation 8. It is important to note while $SrCO_3$ formation is observed, it is not possible in the set of experiments reported in the present work to distinguish between direct formation of $SrCO_3$ from the perovskite and the formation of $SrCO_3$ from SrO originally ex-solved from the perovskite phase through surface segregation and precipitation.

The standard Quantum Espresso software package [10] was utilized to compute the ground state energy. Ultrasoft pseudopotentials and generalized gradient approximation (GGA) for the exchange-correlation functional with the on-site Hubbard repulsion U (GGA + U) [11] corrections were used in this calculation. We applied Standard Coulomb repulsion parameter of U = 5 eV and exchange parameter of J = 1 eV to the 3d orbitals of the B-site transition metals including Fe and Co [12]. The energy cutoff was set to be 450 eV. The spin polarization effects were fully applied in the simulation. Figure 6 shows a representative supercell with the periodic boundary conditions applied along all the three x, y and z directions. The supercell was built for $La_{0.75}Sr_{0.25}Co_{0.25}Fe_{0.75}O_3$ containing a total of 40 atoms. Monkhorst-Pack k-point mesh was set to be 2×2×2 in the first Brillouin zone for the total energy calculations [13]. The computed equilibrium lattice constant of such a cubic perovskite oxide was 3.91 Å, which is consistent with the experimental value of 3.925 Å for $La_{0.6}Sr_{0.4}Co_{0.2}Fe_{0.8}O_3$ [14]. A large vacuum of 10 Å is used and the atoms on the bottom layer were fixed at their bulk geometry to mimic the surface phase.

The crystal structure of $SrCO_3$ is orthorhombic [15]. The chemical potential for CO_2 calculated was simply adopted from the NIST Webbook [16]. Since it is well known that the vibrational

entropy changes of solids in these types of heterogeneous catalytic reactions are much smaller than the gas-phase entropy and the configurational entropy contributions, only the configurational entropy was considered.

Four separate cases were calculated. Two oxygen vacancy concentrations in LSCF, corresponding to $\delta = 0$ and 0.125, were considered, each exposed to two CO_2 partial pressures of 3.6×10^{-4} atm (CO_2 partial pressure in atmospheric air) and 0.3 atm. In all cases, the free energy change of Eq. 9 is presented in PO_2 versus T plots (Figure 7). The dashed lines in the figures are the loci of $\Delta G = 0$. To the left of the dashed line (blue area), $\Delta G < 0$, implying there is a thermodynamic driving force for $SrCO_3$ formation. To the right of the dashed line (red area), $\Delta G > 0$, it implies that $SrCO_3$ formation is not stable. The results show that for both vacancy concentrations, increasing CO_2 the partial pressure moves the dashed line move towards high temperature values, thereby increasing the temperature range over which $SrCO_3$ formation is stable. This again indicates CO_2 in the atmosphere provides additional thermodynamic driving force for the forward reaction in Eq. 9, and thus enhances the kinetics of Sr surface segregation. These two mechanisms both indicate enhanced kinetics and at this point it is not possible to distinguish which is prevalent.

Interestingly, Figure 7 shows that increasing the oxygen vacancy concentration also moves the dashed line to the right, thereby increasing the range of $SrCO_3$ stability. Although the exact reason for this is not known, it is speculated that the introduction of vacancies destabilizes the perovskite phase, making it easier to form surface phases. Of course, given that the simulated composition is not identical to the actual composition, and that the near surface oxygen vacancy concentration is not known; the DFT results should not be taken as quantitatively accurate. Nevertheless, the results do explain the trends that are experimentally observed.

For the CO_2-free case, the formation of some $SrCO_3$ surface phase (Figure 5b) is unexpected. This can be possibly attributed to trace CO_2 in the gases. The purities of the gases used in the experiments are: oxygen > 99.5%, nitrogen > 99.9995%, and carbon dioxide > 99.95%.

Interestingly, Figure 4 shows that the highest Sr/(Sr+La) ratio in the CO_2-free case (above 0.5) is higher than that in high-CO_2 case (below 0.5). Since after 9 hours of annealing, the Sr segregation is still evolving for CO_2-free case, while it seems to saturate for the high-CO_2, a

relevant question is whether the saturation in high-CO_2 case is due to significant reduction in the perovskite surface due to surface phase formation.

In order to address this issue, AFM analyses of the sample surfaces after annealing were carried out. The AFM images are shown in Figures 8a and 8b. The figures shows that the surface precipitates in 30% CO_2 case are significantly larger than those in the CO_2-free case, resulting in surface area coverage ratio of 61.3% versus 12.2%, respectively. This supports the conjecture that in the high-CO_2 case, the surface is indeed highly covered by the newly formed surface phases. These surface phases can act as a diffusion barrier, thereby reducing the effective area for Sr surface segregation and reaching a steady state after 2 hours of annealing.

5. Conclusions

This study demonstrates that the presence of CO_2 in the atmosphere enhances the kinetics of surface Sr segregation in LSCF-6428 thin films at 800°C. The results suggest that the formation of $SrCO_3$ increases segregation kinetics and allows Sr surface segregation to reach a steady state significantly faster. It appears that this steady state is not due to the surface reaching thermodynamic equilibrium, but due to blocking of the perovskite surface by the surface phases.

Acknowledgments

This work is supported through the DOE SECA program under Grant DEFC2612FE0009656. A portion of the research was performed at EMSL, a national scientific user facility sponsored by the Department of Energy's Office of Biological and Environmental Research and located at Pacific Northwest National Laboratory.

References

[1] H. Ullmann, N. Trofimenko, F. Tietz, D. Stover, and A. Ahmad-Khanlou, Correlation between thermal expansion and oxide ion transport in mixed conducting perovskite-type oxides for cathodes, Solid State Ionics 138 (2000) 79–90.

[2] S.P. Simner, M.D. Anderson, M.H. Engelhard and J.W Stevenson, Degradation Mechanisms of La–Sr–Co–Fe–O_3 SOFC Cathodes, Electrochemical and solid-state letters, 9 (2006) A478-A481.

[3] E. Bucher and W. Sitte, Long-term stability of the oxygen exchange properties of $(La, Sr)_{1-z}$ (Co, Fe) $O_{3-\delta}$ in dry and wet atmospheres, Solid State Ionics, 192(1), pp 480-482. (2011).

[4] P.A.W. Van Der Heide, Systematic x‐ray photoelectron spectroscopic study of $La_{1-x}Sr_x$‐based perovskite‐type oxides, Surface and interface analysis 33 (2002) 414-425.

[5] S.R. Bishop, K.L. Duncan and E.D. Wachsman, Surface and bulk defect equilibria in strontium-doped lanthanum cobalt iron oxide, Journal of the Electrochemical Society 156 (2009) B1242-B1248.

[6] D. Oh, D. Gostovic, and E.D. Wachsman, Mechanism of $La_{0.6}Sr_{0.4}Co_{0.2}Fe_{0.8}O_3$ Cathode Degradation, Journal of Materials Research 27 (2012) 1992-1999.

[7] J.N. Davis, Y. Yu, D. Cetin, K.F. Ludwig, U.B. Pal, S. Gopalan, and S.N. Basu, Surface Segregation and Phase Formation in Thin Films of SOFC Cathode Materials, Proceedings of Energy Technology 2014: High-temperature Material Systems for Energy Conversion and Storage, TMS, (2014) 247-258.

[8] Y. Tanaka, A. Momma, K. Sato and T. Kato, Improvement of Electrical Efficiency of Solid Oxide Fuel Cells by Anode Gas Recycle, ECS Transactions, 30 (2011) 145-150.

[9] J. C.Woicik, B. Ravel, D. A.Fischer, and W. J. Newburgh, Performance of a four-element Si drift detector for X-ray absorption fine-structure spectroscopy: resolution, maximum count rate, and dead-time correction with incorporation into the ATHENA data analysis software, Journal of synchrotron radiation, 17 (2010) 409-413.

[10] P. Giannozzi, S. Baroni, N. Bonini, M. Calandra, R. Car, C. Cavazzoni, et al., QUANTUM ESPRESSO: a modular and open-source software project for quantum simulations of materials., J. Phys. Condens. Matter. 21 (2009) 395502.

[11] A. Liechtenstein, V. Anisimov, J. Zaanen, Density-functional theory and strong interactions: Orbital ordering in Mott-Hubbard insulators, Phys. Rev. B. 52 (1995) 5467–5471.

[12] Y.-L. Lee, J. Kleis, J. Rossmeisl, D. Morgan, Ab initio energetics of LaBO3(001) (B=Mn , Fe, Co, and Ni) for solid oxide fuel cell cathodes, Phys. Rev. B. 80 (2009) 224101.

[13] H. Monkhorst, J. Pack, Special points for Brillouin-zone integrations, Phys. Rev. B. 13 (1976) 5188–5192.

[14] J.S. Hardy, J.W. Templeton, D.J. Edwards, Z. Lu, J.W. Stevenson, Lattice expansion of LSCF-6428 cathodes measured by in situ XRD during SOFC operation, J. Power Sources. 198 (2012) 76–82.

[15] http://www.handbookofmineralogy.org/pdfs/strontianite.pdf

[16] http://webbook.nist.gov/

Figures

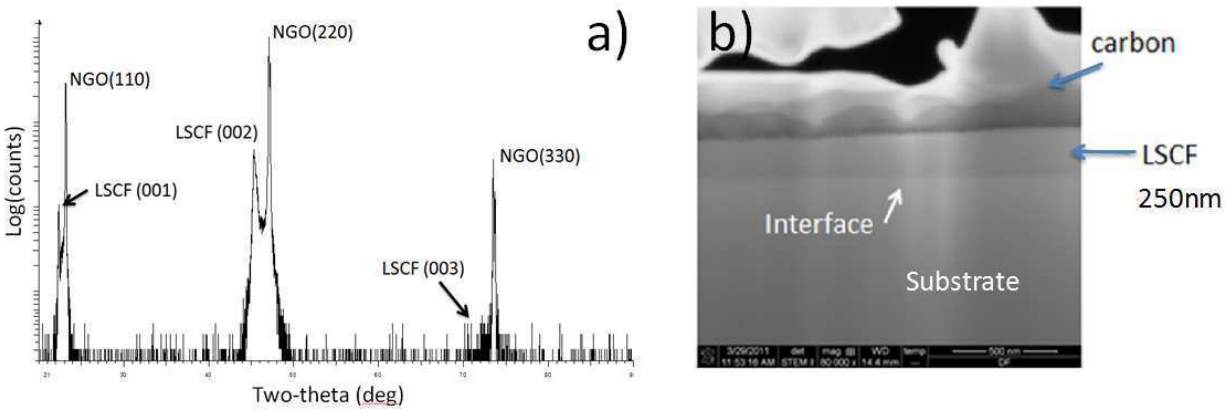

Figure 1. (a) XRD and (b) FIB-SEM of (001) LSCF-6428 thin film on (110) NGO substrate.

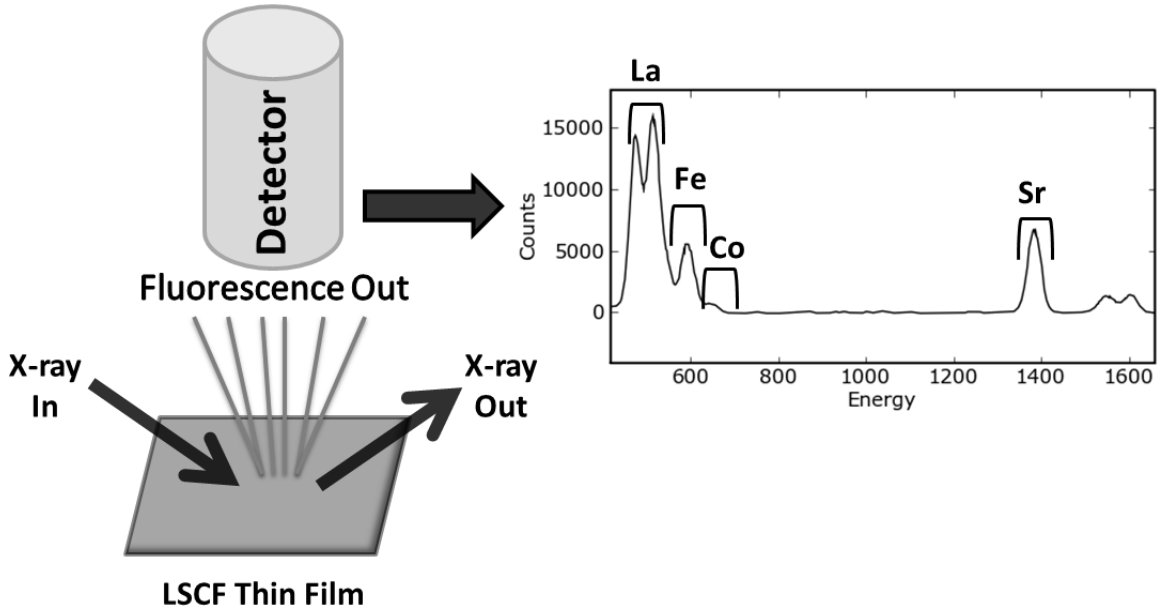

Figure 2. Schematic of a typical TXRF measurement showing fluorescence peaks corresponding to the different elements in LSCF.

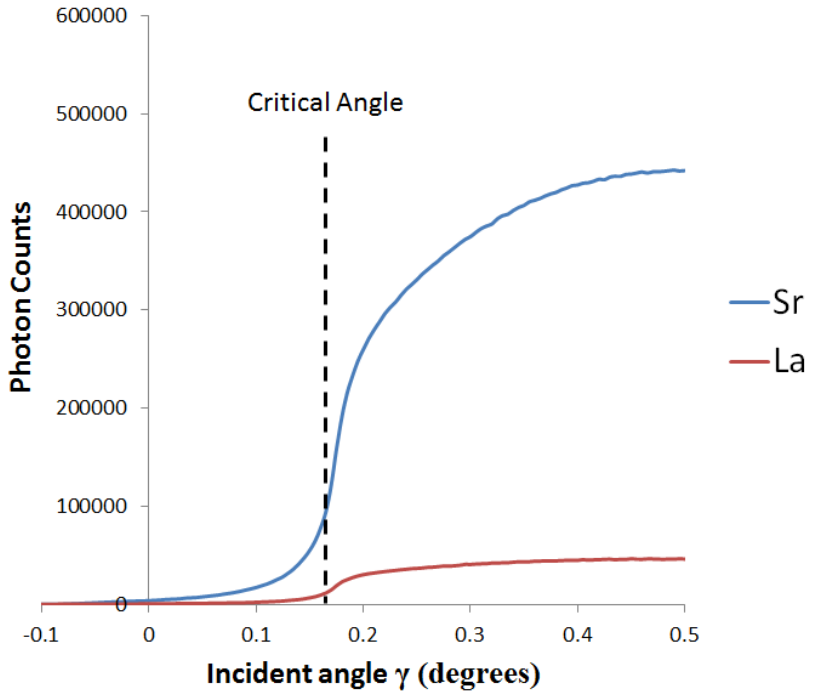

Figure 3. Typical TXRF raw data for LSCF-6428 thin film. The dashed line marks the position of the critical angle.

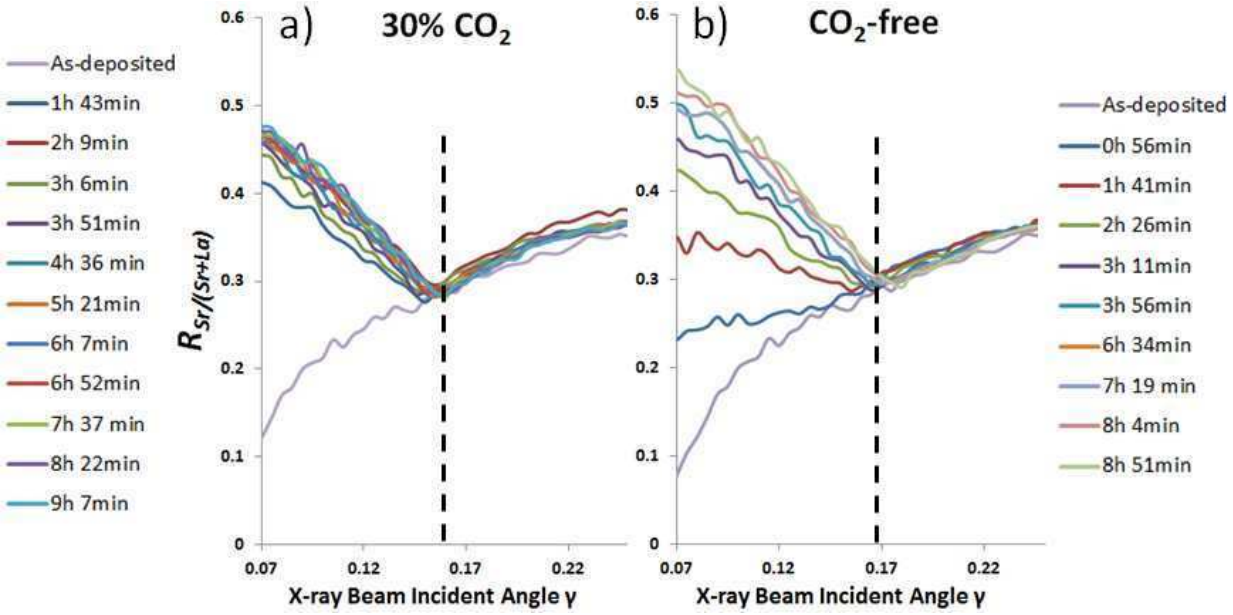

Figure 4. Real-time TXRF data for LSCF-6428 plotted as Sr/(Sr+La) ratio versus x-ray beam incident angle. The plots are from data collected at (a) 800°C in 30% CO_2, 21% O_2 and 49% N_2 for 9 hours and 7 minutes and at (b) 800°C in 21% O_2 and 79% N_2 for 8 hours and 51 minutes.

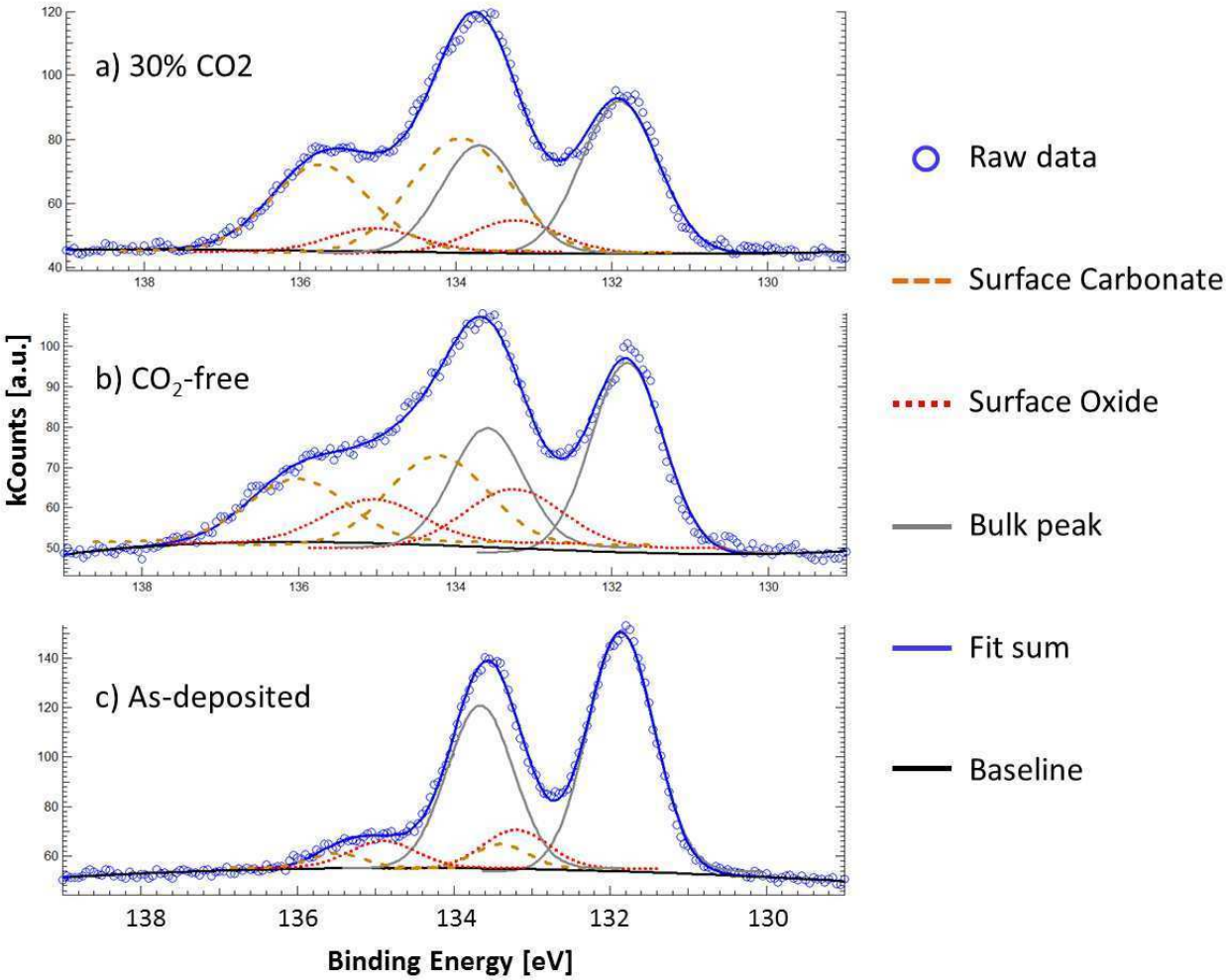

Figure 5. Sr 3d peaks of a) 30% CO_2-annealed, b) CO_2-free annealed and c) as-deposited films obtained by HAXPES measurements. The data is fit to a combination of a surface oxide (SrO), a surface carbonate ($SrCO_3$) and a bulk perovskite (LSCF) phase.

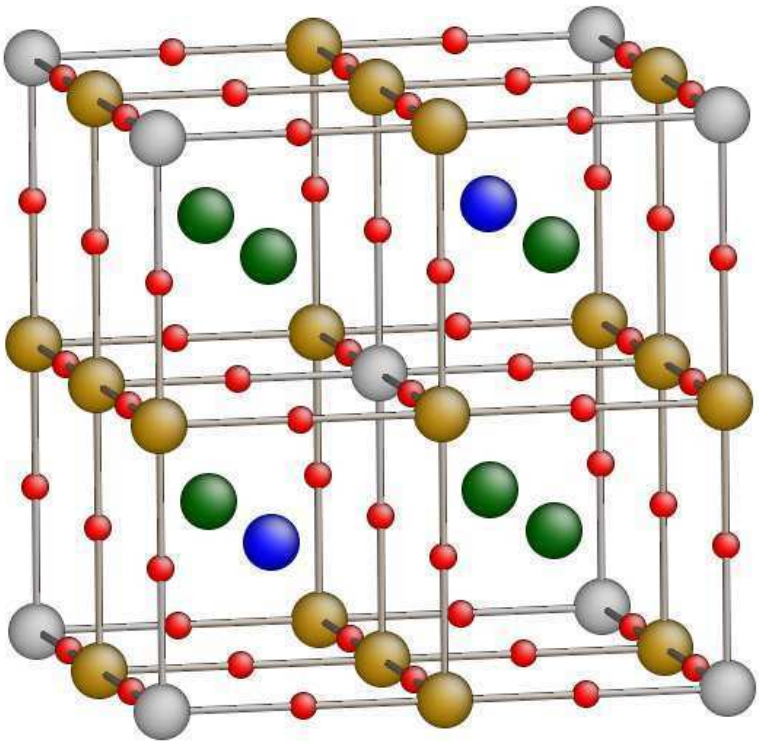

Figure 6. Representative 2X2X2 supercell of $La_{0.75}Sr_{0.25}Co_{0.25}Fe_{0.75}O_3$ used for the DFT calculations.

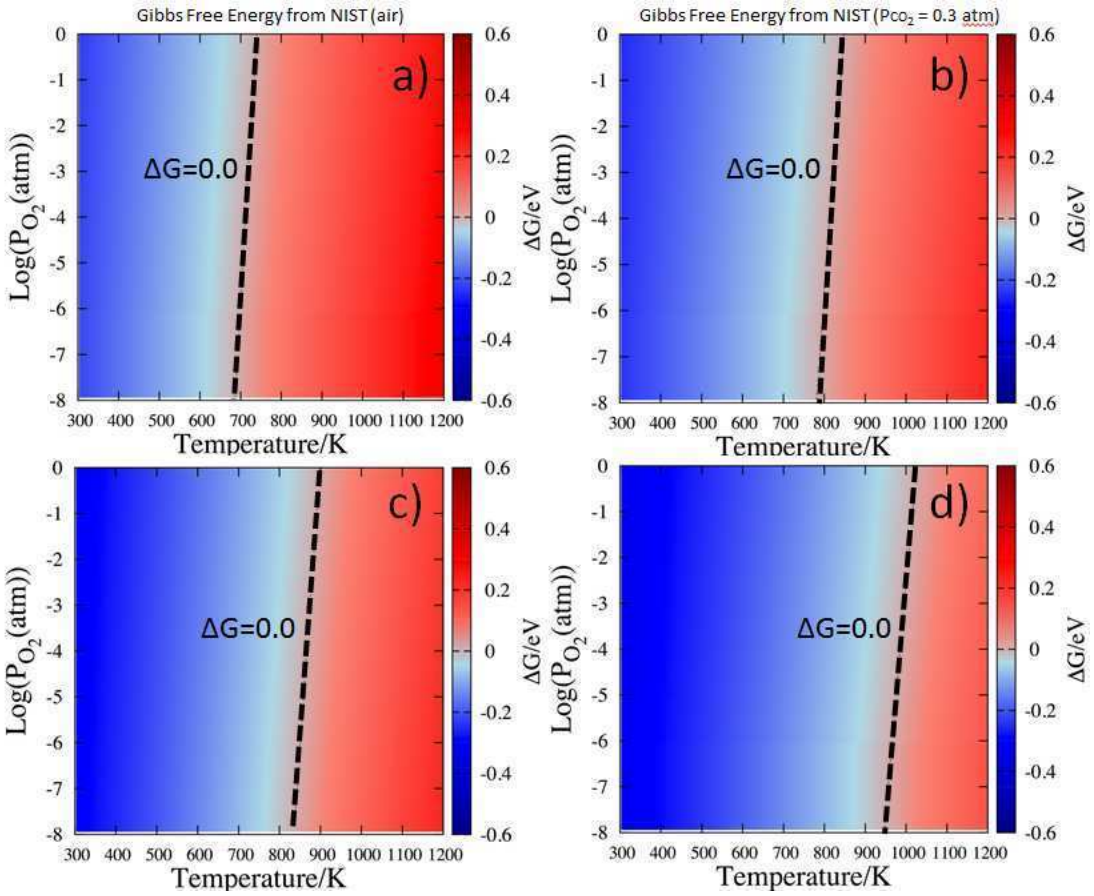

Figure 7. Calculated phase diagrams for the above reaction plotted as log(pO_2) versus temperature, where a) δ =0, pCO_2=360 ppm, b) δ =0, pCO_2=0.3 atm, c) δ =0.125, pCO_2=360 ppm, and d) δ =0.125, pCO_2=0.3 atm.

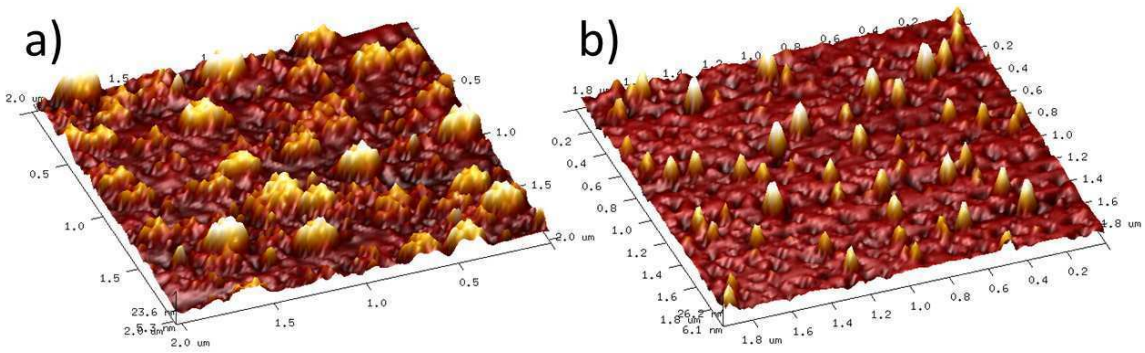

Figure 8. AFM 3-D images of the surface of post-annealed LSCF-6428 samples in a) high-CO_2 environment and b) CO_2-free environment.

Reprinted from:Y.Yu, H.Luo, D.Cetin. X.Lin, K.Ludwig, U.Pal, S.Gopalan, and S.Basu, “Effect of atmospheric CO_2 on surface segregation and phase formation in $La_{0.6}Sr_{0.4}Co_{0.2}Fe_{0.8}O_{3-\delta}$ thin films”, *App. Surf. Sci.*, 323 (2014) 71-77 with permission from Elsevier.

Predicting oxygen vacancy non-stoichiometric concentration in perovskites from first principles

Heng Luo[a], Yongwoo Shin[a,b], Yang Yu[b], Deniz Cetin[b], Karl Ludwig[b,c], Uday Pal[a,b], Soumendra N. Basu[a,b], Srikanth Gopalan[a,b], Xi Lin[a,b,*]

[a] *Department of Mechanical Engineering, Boston University, Boston, MA 02215, USA*
[b] *Division of Materials Science and Engineering, Boston University, Brookline, MA 02446, USA*
[c] *Department of Physics, Boston University, Boston, MA 02215, USA*

Abstract

Formation of oxygen vacancies by introducing various mixed-valent cation dopants is a common practice to improve the cathode performance in solid oxide fuel cells. A computational procedure is developed in this work to predict the equilibrium oxygen vacancy non-stoichiometric concentrations at experimentally relevant temperatures and oxygen partial pressures for both bulk and surface oxide phases. The calculations are based on the first-principles density functional theory and a constrained free-energy functional. Quantitative agreements are found by direct comparisons to the thermogravimetry and solid electrolyte coulometry measurements for the strontium-doped lanthanum cobalt iron oxides at different compositions. Our results indicate that the oxygen vacancies are energetically stabilized at surfaces for all temperatures and all oxygen partial pressures, while such surface stabilization effects become stronger at higher temperatures and lower oxygen partial pressures.

Keywords: Solid oxide fuel cells, perovskite oxides, oxygen vacancy, non-stoichiometric concentration, first-principles density functional theory, free-energy functional

*Corresponding author
Email address: linx@bu.edu (Xi Lin)

1. Introduction

Because of the unique combination of mixed ionic and electronic conductances (MIEC)[1, 2, 3, 4], perovskite oxides have been widely used as the cathode materials for solid oxide fuel cells (SOFC)[5]. Typical A-site cations in these perovskite cathode materials contain rare and alkaline earth elements such as La, Sr, Ca, and Ba, and typical B-site cations consist of reducible transition metal elements such as Mn, Fe, Co, and Ni[6]. Over the past two decades, extensive scientific research efforts have been focused on optimizing the materials compositions in lanthanum strontium transition metal oxides such as $La_{1-x}Sr_xCo_yFe_{1-y}O_{3-\delta}$ (LSCF) to improve the catalytic performance in oxygen reduction reactions, chemical and mechanical stabilities at high temperatures, and thermal expansion properties, as well as to lower the materials and processing costs[7, 8].

It has been well recognized that the MIEC of these perovskite cathode materials may be modified through controlling the oxygen non-stoichiometry $O_{3-\delta}$ concentration δ [9], which in turn is a complicated function of the materials compositions, temperature T, and oxygen partial pressure P_{O_2}. These non-stoichiometric anion vacancy defects were often introduced into perovskites in the growth, annealing, and redox reaction processes. However, if the resulting dopant and defect concentrations were not thermodynamically favorable, metastable microstructures could undergo degradations[10] and consequentially affect the overall device performance.

Experimentally, oxygen vacancy non-stoichiometric concentrations in LSCF were measured through oxygen mass changes using the thermo-gravimetry (TG)[9] and solid electrolyte coulometry (SECM) [11] techniques. Various empirical defect models[9, 12, 13] were introduced to explain these measurements, but all shared the following common problems. Firstly, all the cation and anion defects were treated as classical particles existing only in their pre-assigned integer valence states and only on the lattice sites such that the quantum nature of electrons and holes was completely ignored. Secondly, these defect models typically required three or four empirical fitting parameters in the forms of enthalpy, entropy, or equilibrium constants. But these fitted thermodynamical functions did not have any explicit temperature and pressure dependences. Thirdly, although the importance of surface defects were often acknowledged in the perovskite oxide literatures[9, 13], these existing empirical defect models [9, 12, 13] did not consider any surface effects. In this work, we present a first-principles density functional theory (DFT)

based free-energy approach to predict the oxygen vacancy non-stoichiometric concentrations $O_{3-\delta}$ for the well documented LSCF system. In this new approach, the cation and anion defects are allowed to displace away from well-defined lattice sites, and their valence states are the natural consequence of continuous wave function and charge distributions. With only one single excess Gibbs free-energy parameter describing the non-ideal solution effects which can be estimated from existing experimental measurements, we expect that the same numerical procedures descried in this work for LSCF can also be applicable to other perovskite oxide materials. To the best of our knowledge, our present approach is the only model that explicitly incorporate the essential surface effects on the oxygen vacancy non-stoichiometric concentrations.

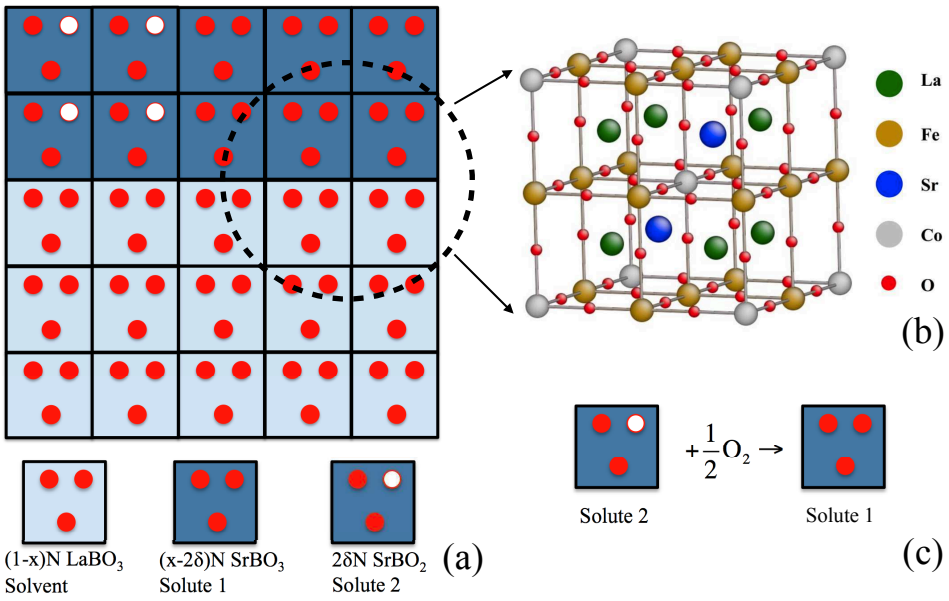

Figure 1: (a) Schematic supercell ensemble, where the dark and light blue cells represent the Sr and La unit cells, respectively. A red filled circle indicates that the corresponding oxygen site is filled with an oxygen atom, and an empty red circle represents an oxygen vacancy site. The chance of forming two oxygen vacancies in one single unit cell is ignored. (b) Representative $2 \times 2 \times 2$ supercell of $La_{0.75}Sr_{0.25}Co_{0.25}Fe_{0.75}O_3$ used in our DFT calculations. (c) Because the oxygen vacancy formation energy in a La unit cell is much greater (> 1.2 eV) than that in a Sr unit cell, the $LaBO_3$, $SrBO_3$, and $SrBO_2$ cells are treated in our free-energy model as the Solvent, Solute 1, and Solute 2, respectively.

2. Computational details

Electronic-structure calculations based on the first-principles DFT provides a generic and powerful tool for predicting many important thermodynamic and kinetic properties of complex oxides[14, 15, 16, 17]. The ground state energy calculations are performed using the standard Quantum Espresso software package[18], which gives all the equilibrium crystal structures, atomic geometries, vibrational entropies under the harmonic oscillator approximation, and electronic wave function and density distributions.

We used plane waves as the basis set with an energy cutoff of 450 eV, ultrasoft pseudopotentials, and generalized gradient approximation (GGA) for the exchange-correlation functional with the on-site Hubbard repulsion U (GGA + U)[19] corrections. Standard Coulomb repulsion parameter U = 5 eV and exchange parameter J = 1 eV are applied to the $3d$ orbitals of the B-site transition metals including Fe and Co[14]. The spin polarization effects are fully treated in all the calculations. A representative supercell with the periodic boundary conditions applied along all the three x, y, and z directions is given in Fig. 1(b) for $La_{0.75}Sr_{0.25}Co_{0.25}Fe_{0.75}O_3$ which contain a total of 40 atoms. A corresponding $2 \times 2 \times 2$ Monkhorst-Pack k-point mesh in the first Brillouin zone was used for the total energy calculations.[20]. The equilibrium lattice constant of such a cubic perovskite oxide is 3.91 Å computed by DFT, consistent with the experimental value of 3.925 Å for $La_{0.6}Sr_{0.4}Co_{0.2}Fe_{0.8}O_3$[21]. To mimic the surface phase, a large vacuum of 10 Å is used and the atoms on the bottom layer are fixed at their bulk geometry.

Going beyond the total energy calculations directly from DFT, we need to construct a free-energy functional to obtain the oxygen vacancy non-stoichiometry concentration as a function of T and P_{O_2}. As shown in Fig. 1(a), a macroscopic sample LSCF perovskite oxide may be represented as an ensemble of N cubic perovskite unit cells. In each unit cell, there are one A atomic site, one B atomic site, and three oxygen atomic sites. For a LSCF sample with a Sr molar dopant fraction of x, there are xN Sr-containing perovskite unit cells and $(1-x)N$ La-containing perovskite unit cells, corresponding to the dark blue and light blue unit cells shown in Fig. 1(a) respectively.

Because it is highly energetically unfavorable to create oxygen vacancies in the La-containing cells as compared to the Sr-containing cells and it is both energetically and entropically unfavorable to create two oxygen vacancies in one single Sr-containing cell, we can further divide the LSCF supercell

ensemble of Fig. 1(a) into three different categories, $(1-x)N$ $LaBO_3$ as the Solvent, $(x-2\delta)N$ $SrBO_3$ as the Solute 1, and $2\delta N$ $SrBO_2$ as the Solute 2. Therefore, the oxygen vacancy formation can only occur between the Solute 1 and Solute 2, as shown in Fig. 1(c). Here the charge neutrality condition is enforced between the Sr dopants and O vacancies as

$$[\mathrm{Sr}'_{\mathrm{La}}] = 2[\mathrm{V}^{\bullet\bullet}_{\mathrm{O}}]. \tag{1}$$

Following such an LSCF defect ensemble representation as shown in Fig. 1, we can express the overall reaction Gibbs free-energy

$$\Delta G = \Delta H - T\Delta S \tag{2}$$

as the sum of the reaction enthalpy

$$\Delta H = H_{\mathrm{Solute1}} - H_{\mathrm{Solute2}} - \frac{1}{2}H_{\mathrm{O_2}} \tag{3}$$

directly from DFT and the reaction entropy

$$\Delta S = \Delta S_{\mathrm{solid}} - \frac{1}{2}\Delta S_{\mathrm{gas}} = (\Delta S_{\mathrm{config}} + \Delta S_{\mathrm{vib}}) - \frac{1}{2}\Delta S_{\mathrm{O_2}}. \tag{4}$$

As shown in Eq. (4), the latter consists of the configurational entropy and vibrational entropy contributions of the solids, as well as the entropy contribution of the gas-phase molecules. Assuming the ideal mixing of all the different supercells in Fig. 1(a), we have

$$\Delta S_{\mathrm{config}} = -k_{\mathrm{B}}[2\delta\ln(2\delta) + (x-2\delta)\ln(x-2\delta)]. \tag{5}$$

Non-ideal free-energy contributions to both the enthalpy term of Eq. (3) and the configurational entropy term of Eq. (5) can be obtained by comparing to real experimental measurements, as to be discussed below.

At experimentally relevant temperatures and pressures, since the vibrational entropy contribution ΔS_{vib} to both the thermodynamic[22, 23, 24] and kinetic[25] properties in typical heterogeneous chemical reactions are much smaller than the other two entropy terms, ΔS_{vib} will be neglected in this work for simplicity. The gas-phase $\Delta S_{\mathrm{O_2}}$ can be either computed from DFT via the canonical transformation of phonons fed to the standard ideal gas, rigid rotor, and harmonic oscillator partition functions[24] or simply adapted from the NIST Webbook[26] as in this work. Their differences in $\Delta S_{\mathrm{O_2}}$ at

experimentally relevant temperatures are typically negligible[24]. Finally, by combining Eqs. (2)-(5), we find an expression for ΔG as

$$\Delta G = \Delta H - T\Delta S_{\mathrm{config}} + \frac{1}{2}T\Delta S_{\mathrm{O_2}}. \tag{6}$$

When the chemical reaction of Fig. 1(c) reaches thermal equilibrium, the reaction equilibrium constant K_{eq} becomes

$$K_{\mathrm{eq}} = \frac{a_{\mathrm{Solute1}}}{a_{\mathrm{Solute2}}a_{\mathrm{O_2}}{}^{\frac{1}{2}}} = \exp\left(-\frac{\Delta G}{\mathrm{R}T}\right), \tag{7}$$

where R is the universal gas constant and the corresponding activities can be written as

$$a_{\mathrm{Solute1}} = \gamma_{\mathrm{Solute1}} \times (x - 2\delta), \tag{8}$$

$$a_{\mathrm{Solute2}} = \gamma_{\mathrm{Solute2}} \times (2\delta), \tag{9}$$

and

$$a_{\mathrm{O_2}} = \frac{P_{\mathrm{O_2}}}{p^0}, \tag{10}$$

where p^0 is the standard 1 atmosphere (atm) reference state.

Defining the activity coefficient ratio $\gamma_{\mathrm{r}} = \gamma_{\mathrm{Solute1}}/\gamma_{\mathrm{Solute2}}$, we can rewrite the equilibrium constant equation as

$$\begin{aligned}\gamma_{\mathrm{r}}\frac{x-2\delta}{2\delta} &= \exp\left[-\frac{\Delta G}{\mathrm{R}T}\right]\left[\frac{P_{\mathrm{O_2}}}{p_0}\right]^{\frac{1}{2}} \\ &= \exp\left[-\frac{\Delta H}{\mathrm{R}T} + \frac{\Delta S_{\mathrm{config}}}{\mathrm{R}} - \frac{\Delta S_{\mathrm{O_2}}}{2\mathrm{R}}\right]\left[\frac{P_{\mathrm{O_2}}}{p_0}\right]^{\frac{1}{2}}.\end{aligned} \tag{11}$$

Here the complicated activity coefficient ratio, which is related to the excess Gibbs energy beyond the ideal solution model, will be estimated from the experimentally measured δ data as to be discussed below.

3. Results and discussion

The thermodynamic energetics computed by DFT were given as follows

$$\begin{aligned}H(\delta) = H_{\mathrm{La_{1-x}Sr_xCo_yFe_{1-y}O_{3-\delta}}} + \frac{\delta}{2}H_{\mathrm{O_2}} \\ - H_{\mathrm{La_{1-x}Sr_xCo_yFe_{1-y}O_3}}(\mathrm{Bulk}),\end{aligned} \tag{12}$$

where the perfect bulk phase without vacancies was chosen to be the energy reference. Fig. 2 shows the DFT vacancy formation energy for one particular LSCF composition $La_{0.75}Sr_{0.25}Co_{0.25}Fe_{0.75}O_{3-\delta}$. It is clear that the formation of surface vacancy is much lower than that in the bulk phase. Such a direct correlation between the vacancy formation and the free surface is consistent with the experimental observed segregations near the LSCF surfaces[27].

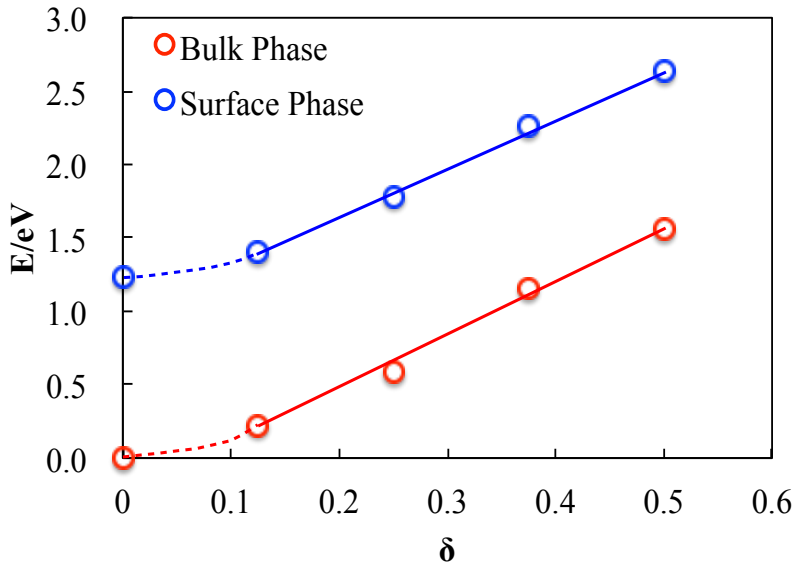

Figure 2: Vacancy formation energy of $La_{0.75}Sr_{0.25}Co_{0.25}Fe_{0.75}O_{3-\delta}$ as a function of the vacancy concentration δ is computed by DFT for both the bulk (red) and surface (blue) phases. The perfect bulk phase is used as the common energy reference.

Inserting the DFT enthalpy results of Fig. 2 into Eq. (11), we can iteratively solve for the oxygen vacancy non-stoichiometric concentrations as a function of P_{O_2} for both the bulk and surface phases, plotted in Fig. 3 as the solid and dashed lines respectively. Together shown in Fig. 3 are the experimental TG (red circles)[9] and SECM (blue crosses) [11] data at four different temperatures T = 873K, 973K, 1073K and 1173K. It is clear that the experimental data are located inside of the shaded area between the bulk phase limit and the surface phase limit, which indicates that the experimental data is a combination of the bulk and surface phases and the two samples from two different groups are likely to have slightly different

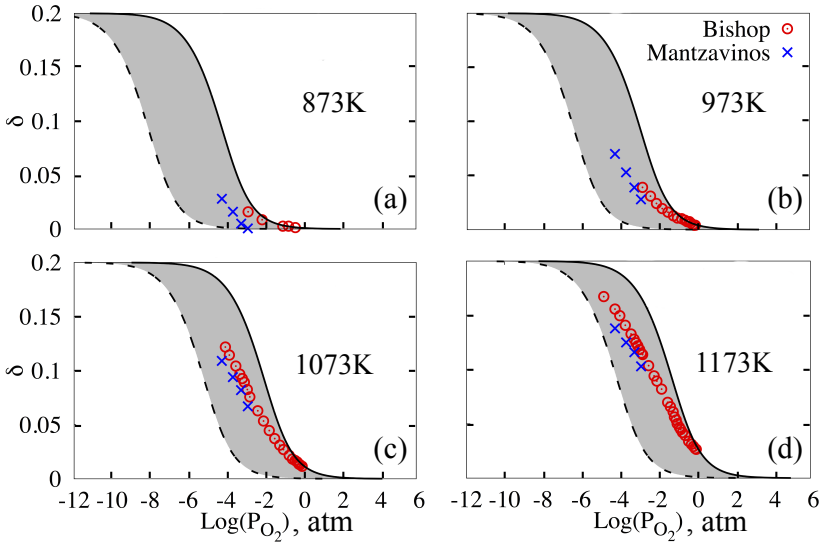

Figure 3: Oxygen vacancy concentration δ as a function of oxygen partial pressure P_{O_2} at four different temperatures T. The dashed and solid lines represent the calculated bulk and surface phase limits by DFT, respectively. The experimental data, TG (red circles) by Bishop et al.[9] and SECM (blue crosses) by Mantzavinos et al.[11], are located in the shaded area between the computed surface and bulk phase limits. As the vacancy concentration increases, the experimental data gradually approach from the surface limit to the bulk limit. Note that due to the computational supercell limitation, LCSF with a slightly different composition is used in the DFT calculations $La_{0.75}Sr_{0.25}Co_{0.25}Fe_{0.75}O_{3-\delta}$ as compared to the experimental sample of $La_{0.6}Sr_{0.4}Co_{0.2}Fe_{0.8}O_{3-\delta}$ (LSCF 6428).

bulk-to-surface ratios. It is important to note that since the vacancy formation energy at surfaces are much less than that in the bulk phase (Fig. 2). Therefore, multiple-parameter fitting with no explicit surface dependences in all existing empirical models may not necessarily have any physical meanings. The essential role of surfaces on many thermodynamic properties of these perovskite oxides has been well acknowledged in literatures[9].

At any fixed temperature among all the four temperatures shown in Fig. (3), as P_{O_2} decreases the oxygen vacancy concentration δ not only increases as expected, but also gradually switches from the bulk phase limit towards the surface phase limit. This new feature was missing in all the previous empirical models[9]. Physically, this trend implies that when P_{O_2} is high, there are only

a small quantity of vacancies in the entire system, and since vacancies prefer the surface face (Fig. 2) they would prefer to be close to the surface phase. On the other hand, when the P_{O_2} is low, more and more imperfect unit cells appear in the system. Because the number of the imperfect unit cells in the surface phase is limited, more and more imperfect unit cells will be located toward the bulk phase such that the experimentally measured oxygen vacancy concentration δ switches toward the bulk phase limit as shown in Fig. 3. Overall, the DFT results show good agreement with the experimental data within one single unknown physical parameter, the activity coefficient ratio γ_r of Eq. (11), which indicates that the calculated DFT energetics and the estimated reaction model are capable of describing the complicated defect chemistry of LSCF.

Additionally, we can reformulate such a complicated activity coefficient ratio of Eq. (11) into the excess Gibbs free energy formalism due to the non-ideal mixing effects ignored in Fig. 1. Namely,

$$\gamma_r = \exp\left[\frac{\Delta G_{\text{non-ideal}}}{\mathrm{R}T}\right] = \exp\left[\frac{\Delta H_{\text{non-ideal}}}{\mathrm{R}T}\right]\exp\left[\frac{\Delta S_{\text{non-ideal}}}{\mathrm{R}}\right] \tag{13}$$

Indeed, plotting $\log(\gamma_r)$ versus $1/T$ in Fig. 4, we find such a linear relationship is confirmed.

Therefore, combining Fig. (3), Fig. (4) and Eq. (11), it is clear that the LSCF data from both the TG and SECM measurements are a combination of vacancies from both the bulk phase and the surface phase. Moreover, we can esimtate the surface phase fraction of the overall vacancy concentration by defining

$$\text{Surface Phase Fraction} = \frac{\delta_{\text{Experiment}} - \delta_{\text{B}}}{\delta_{\text{S}} - \delta_{\text{B}}}. \tag{14}$$

The corresponding results as a function of P_{O_2} are shown in Fig. 5 for two representative temperatures. For both temperatures, the surface phase fraction decreases when the oxygen partial pressure P_{O_2} decreases. Such a surface-to-bulk transition occurs at different P_{O_2} windows for different temperature. In general, it occurs at lower partial pressure values if the temperature is lower as shown in Fig. 5.

Combining the reformulated T-dependent activity coefficient ratio obtained from Fig. 4 and Eq. (11), we can now predict the oxygen vacancy non-stoichiometric concentration δ as a continuous function of T and P_{O_2}. The constant δ contour plots are shown in Fig. 6, where the red, green,

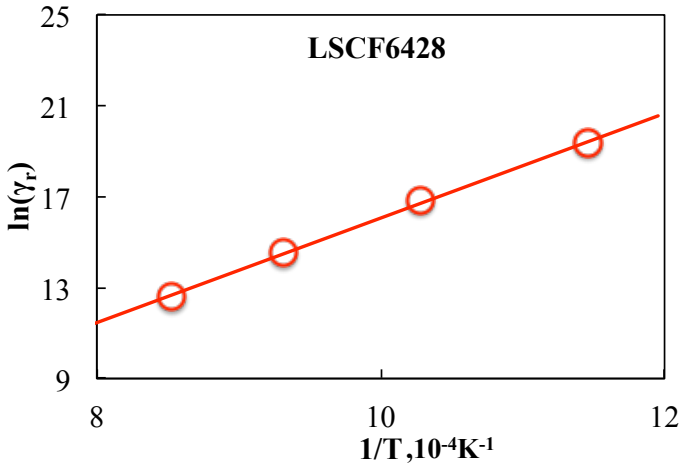

Figure 4: The unknown activity coefficient ratio γ_{r} is reformulated into the Gibbs free energy changes due to non-ideal mixing, as confirmed by the linear relationship between $\log(\gamma_{\mathrm{r}})$ and $1/T$.

and blue lines represent δ= 0.15, 0.10, and 0.05, respectively. Only three iso-value lines of the oxygen vacancy concentration are shown for both the surface and bulk phases to avoid ambiguous overlaps. Using the predicted δ_{B} and δ_{S} contours as the guidelines, we can give a reasonable estimation of the equilibrium δ for real experimental samples.

Using the same computational procedure discussed above, we can also compute the oxygen nonstoichiometric concentrations for LSCF with different materials compositions. Explicitly, Fig. 7 shows the direct comparison of our computed $La_{0.8}Sr_{0.2}Co_{0.2}Fe_{0.8}O_{3-\delta}$ (LSCF8228) bulk and surface limits with the SECM data measured by Mantzavinos[11].

4. Summary and conclusions

A first-principles DFT based computational approach is developed in this work to predict the oxygen vacancy non-stoichiometric concentrations for LSCF as a function of temperature and partial pressure of oxygen. Good agreement with the experimental data are found over the entire relevant temperature and pressure ranges. Our prediction indicates that the oxygen vacancy non-stoichiometric concentrations in real materials samples have contributions from both the surface phase and the bulk phase. The surface

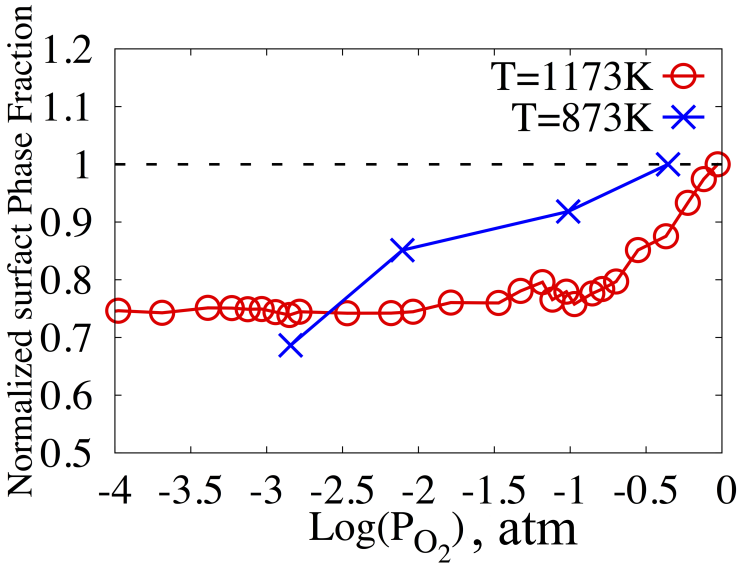

Figure 5: Normalized surface phase fraction versus the oxygen partial pressure P_{O_2} for two representative temperatures. For both temperatures, the surface phase fraction decreases as P_{O_2} decreases. This fast bulk-to-surface crossover occurs at lower partial pressures for lower temperatures.

contributions are stronger at lower temperatures and at higher oxygen partial pressures. The fast surface-to-bulk phase transition occurs at lower partial pressure windows for lower temperatures.

The work is supported by DOE-SECA under Grant DEFC2612FE0009656 and NSF-XSEDE under Grant DMR-0900073.

[1] H. Anderson, Review of p-type doped perovskite materials for SOFC and other applications (1992). doi:10.1016/0167-2738(92)90089-8.

[2] P. Dyer, R. Richards, S. Russek, D. Taylor, Ion transport membrane technology for oxygen separation and syngas production, Solid State Ionics 134 (2000) 21–33.
URL http://www.sciencedirect.com/science/article/pii/S0167273800007104

[3] H. Wang, Y. Cong, W. Yang, Investigation on the partial oxidation of methane to syngas in a tubular $Ba_{0.5}Sr_{0.5}Co_{0.8}Fe_{0.2}O_{3-\delta}$ membrane

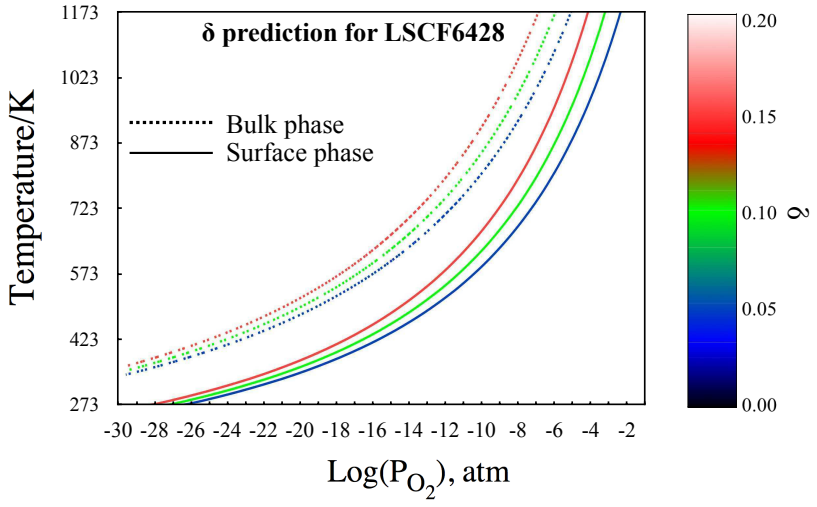

Figure 6: Predicted oxygen vacancy non-stoichiometric concentration δ for LSCF6428 as a function of P_{O_2} and T for both the bulk (solid lines) and surface (dashed) phases. Only three iso-value lines for three different oxygen vacancy concentrations are explicitly shown, red for $\delta = 0.15$, green for $\delta = 0.10$, and blue for $\delta = 0.05$. For experimental samples, the oxygen vacancy non-stoichiometric concentrations δ are between the bulk and surfaced limits.

reactor, Catalysis Today 82 (1-4) (2003) 157–166. doi:10.1016/S0920-5861(03)00228-1.
URL http://linkinghub.elsevier.com/retrieve/pii/S0920586103002281

[4] Y. Liu, X. Tan, K. Li, Mixed Conducting Ceramics for Catalytic Membrane Processing, Catalysis Reviews 48 (2) (2006) 145–198. doi:10.1080/01614940600631348.
URL http://www.tandfonline.com/doi/abs/10.1080/01614940600631348

[5] C. Sun, R. Hui, J. Roller, Cathode materials for solid oxide fuel cells: a review, Journal of Solid State Electrochemistry 14 (7) (2009) 1125–1144. doi:10.1007/s10008-009-0932-0.
URL http://link.springer.com/10.1007/s10008-009-0932-0

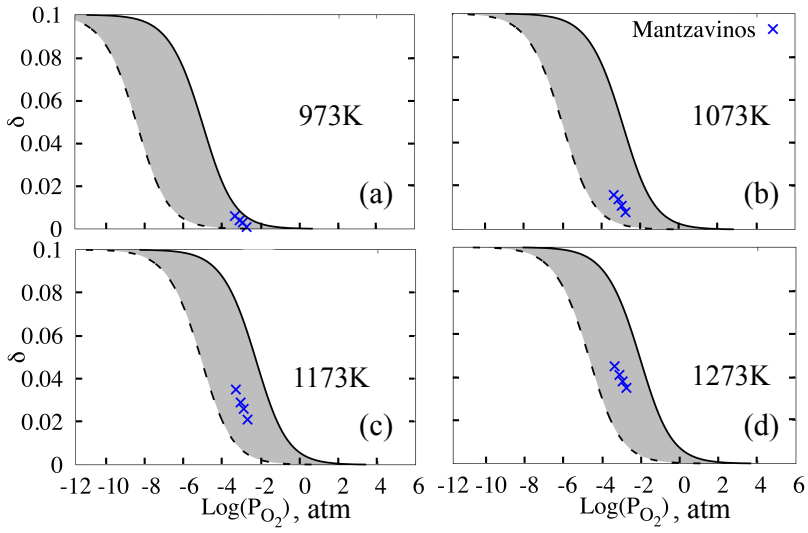

Figure 7: Oxygen vacancy concentration δ as a function of oxygen partial pressure P_{O_2} for LSCF8228. The dashed and solid lines represent the calculated bulk phase and surface phase limits. The experimental data measured by Mantzavinos[11] using the SECM technique are located inside of the shaded area, indicating the real materials samples are combination of these two phases.

[6] M. A. Pena, J. L. G. Fierro, Chemical Structures and Performance of Perovskite Oxides, Chemical Reviews 101.

[7] B. C. H. Steele, Survey of materials selection for ceramic fuel cells, Solid State Ionics 88 (1996) 1223–1234.

[8] V. Dusastre, J. Kilner, Optimisation of composite cathodes for intermediate temperature SOFC applications, Solid State Ionics 126 (1999) 163–174.
URL http://www.sciencedirect.com/science/article/pii/S0167273899001083

[9] S. R. Bishop, K. L. Duncan, E. D. Wachsman, Surface and bulk defect equilibria in strontium-doped lanthanum cobalt iron oxide, Journal of The Electrochemical Society 156 (10) (2009) B1242–B1248, 498IV Times Cited:13 Cited References Count:50. doi:Doi 10.1149/1.3194783.
URL <Go to ISI>://000270133400029

[10] G. Y. Yang, E. C. Dickey, C. A. Randall, M. S. Randall, L. A. Mann, Modulated and ordered defect structures in electrically degraded Ni−$BaTiO_3$ multilayer ceramic capacitors, Journal of Applied Physics 94 (9) (2003) 5990. doi:10.1063/1.1615300.
URL http://scitation.aip.org/content/aip/journal/jap/94/9/10.1063/1.1615300

[11] D. Mantzavinos, A. Hartley, I. S. Metcalfe, M. Sahibzada, Oxygen stoichiometries in $La_{1-x}Sr_xCo_{1-y}Fe_yO_{3-\delta}$ perovskites at reduced oxygen partial pressures, Solid State Ionics 134 (2000) 103–109.

[12] S. Stø len, E. Bakken, C. E. Mohn, Oxygen-deficient perovskites: linking structure, energetics and ion transport., Physical chemistry chemical physics : PCCP 8 (4) (2006) 429–47. doi:10.1039/b512271f.
URL http://www.ncbi.nlm.nih.gov/pubmed/16482285

[13] E. Bakken, T. Norby, S. Stø len, Redox energetics of perovskite-related oxides, Journal of Materials Chemistry 12 (2) (2002) 317–323. doi:10.1039/b106422n.
URL http://xlink.rsc.org/?DOI=b106422n

[14] Y.-L. Lee, J. Kleis, J. Rossmeisl, D. Morgan, Ab initio energetics of $LaBO_3$(001) (B=Mn , Fe, Co, and Ni) for solid oxide fuel cell cathodes, Physical Review B 80 (22) (2009) 224101. doi:10.1103/PhysRevB.80.224101.
URL http://link.aps.org/doi/10.1103/PhysRevB.80.224101

[15] M. J. Gadre, Y.-L. Lee, D. Morgan, Cation interdiffusion model for enhanced oxygen kinetics at oxide heterostructure interfaces., Physical chemistry chemical physics: PCCP 14 (8) (2012) 2606–16. doi:10.1039/c2cp23033j.
URL http://www.ncbi.nlm.nih.gov/pubmed/22270079

[16] Y. A. Mastrikov, R. Merkle, E. A. Kotomin, M. M. Kuklja, J. Maier, Formation and migration of oxygen vacancies in $La_{1-x}Sr_xCo_{1-y}Fe_yO_{3-\delta}$ perovskites: insight from ab initio calculations and comparison with $Ba_{1-x}Sr_xCo_{1-y}Fe_yO_{3-\delta}$., Physical chemistry chemical physics : PCCP 15 (3) (2013) 911–8. doi:10.1039/c2cp43557h.
URL http://www.ncbi.nlm.nih.gov/pubmed/23202751

[17] R. Merkle, Y. A. Mastrikov, E. A. Kotomin, M. M. Kuklja, J. Maier, First Principles Calculations of Oxygen Vacancy Formation and Migration in $Ba_{1-x}Sr_xCo_{1-y}Fe_yO_{3-\delta}$ Perovskites, Journal of The Electrochemical Society 159 (2) (2012) B219. doi:10.1149/2.077202jes.
URL http://jes.ecsdl.org/cgi/doi/10.1149/2.077202jes

[18] P. Giannozzi, S. Baroni, N. Bonini, M. Calandra, R. Car, C. Cavazzoni, D. Ceresoli, G. L. Chiarotti, M. Cococcioni, I. Dabo, A. Dal Corso, S. de Gironcoli, S. Fabris, G. Fratesi, R. Gebauer, U. Gerstmann, C. Gougoussis, A. Kokalj, M. Lazzeri, L. Martin-Samos, N. Marzari, F. Mauri, R. Mazzarello, S. Paolini, A. Pasquarello, L. Paulatto, C. Sbraccia, S. Scandolo, G. Sclauzero, A. P. Seitsonen, A. Smogunov, P. Umari, R. M. Wentzcovitch, QUANTUM ESPRESSO: a modular and open-source software project for quantum simulations of materials., Journal of physics. Condensed matter : an Institute of Physics journal 21 (39) (2009) 395502. doi:10.1088/0953-8984/21/39/395502.
URL http://www.ncbi.nlm.nih.gov/pubmed/21832390

[19] A. I. Liechtenstein, V. I. Anisimov, J. Zaanen, Density-functional theory and strong interactions: Orbital ordering in mott-hubbard insulators, Phys. Rev. B 52 (1995) R5467–R5470. doi:10.1103/PhysRevB.52.R5467.
URL http://link.aps.org/doi/10.1103/PhysRevB.52.R5467

[20] H. J. Monkhorst, J. D. Pack, Special points for brillouin-zone integrations, Phys. Rev. B 13 (1976) 5188–5192. doi:10.1103/PhysRevB.13.5188.
URL http://link.aps.org/doi/10.1103/PhysRevB.13.5188

[21] J. S. Hardy, J. W. Templeton, D. J. Edwards, Z. Lu, J. W. Stevenson, Lattice expansion of LSCF-6428 cathodes measured by in situ XRD during SOFC operation, Journal of Power Sources 198 (2012) 76–82. doi:10.1016/j.jpowsour.2011.09.099.
URL http://linkinghub.elsevier.com/retrieve/pii/S0378775311019355

[22] X. Lin, N. J. Ramer, A. M. Rappe, K. C. Hass, W. F. Schneider, B. L. Trout, Effect of particle size on the adsorption of o and s atoms on pt: A density-functional theory study, Journal of Physical Chemistry B 105 (2001) 7739–7747.

[23] X. Lin, K. C. Hass, W. F. Schneider, B. L. Trout, Chemistry of sulfur oxides on transition metals i. configurations, energetics, orbital analyses, and surface coverage effects of so_2 on pt(111), Journal of Physical Chemistry B 106 (2002) 12575–12583.

[24] X. Lin, W. F. Schneider, B. L. Trout, Chemistry of sulfur oxides on transition metals. ii. thermodynamics of sulfur oxides on platinum(111), Journal of Physical Chemistry B 108 (2004) 250–264.

[25] X. Lin, W. F. Schneider, B. L. Trout, Chemistry of sulfur oxides on transition metals. iii. oxidation of so_2 and self-diffusion of o, so_2, and so_3 on pt(111), Journal of Physical Chemistry B 108 (2004) 13329–13340.

[26] http://webbook.nist.gov/.

[27] S. P. Simner, M. D. Anderson, M. H. Engelhard, J. W. Stevenson, Degradation Mechanisms of $La - Sr - cO - Fe - O_3$ SOFC Cathodes, Electrochemical and Solid-State Letters 9 (10) (2006) A478. doi:10.1149/1.2266160.
URL `http://esl.ecsdl.org/cgi/doi/10.1149/1.2266160`

Reprinted from: H.Luo, Y.Shin, Y.Yu, D.Cetin, K.Ludwig, U.Pal, S.Basu, S.Gopalan, andX.Lin, "Predicting oxygen vacancy non-stoichiometric concentration perovskites from first principles", *App. Surf. Sci.*, 323 (2014) 65-70 with permission from Elsevier.

Surface evolution of lanthanum strontium cobalt ferrite thin films at low temperatures

D. Newby Jr.[1], J. Kuyyalil[1], J. Laverock[1], K.F. Ludwig[1], and K.E. Smith[1,2]
1. *Department of Physics, Boston University, 590 Commonwealth Avenue, Boston, MA 02215*
2. *School of Chemical Sciences and The MacDiarmid Institute for Advanced Materials and Nanotechnology, The University of Auckland, Auckland 1142, New Zealand*

Y. Yu[3], J. Davis[3], S. Gopalan[3], U.B. Pal[3], S.Basu[3,4]
3. *Division of Materials Science and Engineering, Boston University,15 St. Mary's Street, Brookline, MA 02446, USA*
4. *Department of Mechanical Engineering, Boston University, 110 Cummington Street, Boston, MA 02215, USA*

Abstract

The electronic and chemical properties of heteroepitaxial thin films of lanthanum strontium cobalt ferrite have been studied using soft x-ray photoelectron spectroscopy. Specifically, the effect of annealing the films at low temperatures in low partial pressures of oxygen and argon has been investigated. We find that atmospheric surface carbon contamination of the films can be removed with annealing in argon, but are incorporated in the surface with oxygen annealing. Irrespective of the gas used, an insulating phase transition occurs near 300°C due to strontium segregation at the surface. The surface develops more insulating character if annealed with oxygen. Different species are proposed to be responsible for the discrepancy in insulating character.

I. Introduction

In the continued efforts to improve energy resource utilization for the twenty-first century, few technologies hold as much promise as solid oxide fuel cells (SOFCs).[1,2] Perovskite-based fuel cell devices can reliably generate electrical power from a wide variety[3,4] of fossil fuels, using existing infrastructure and with high energy density in a small volume. Critical to the operation of a SOFC is the cathode material, which produces oxygen ions and transports them into the electrode. Indeed, cathode surface and interface modification is one of the primary contributors[5,6] to the operational degradation of an operating fuel cell. Understanding the processes at the cathode is critical to potential improvements and elucidating the factors limiting the life of these devices.

Many high-temperature fuel cells use lanthanum-doped strontium manganite (LSMO) cathodes[7], the reaction kinetics of which are limited to the triple-phase boundary.[8] Overcoming the limitations imposed by the triple-phase boundary would allow for higher energy densities and efficiencies. Mixed ion-electron conductors can transport oxygen ions using more of their surface area, without relying on the electrode interfaces. One of the most promising mixed ion-electron conductors under popular investigation for use as a cathode is lanthanum strontium cobalt ferrite ($La_{0.6}Sr_{0.4}Co_{0.2}Fe_{0.8}O_3$, abbreviated LSCF). LSCF offers high electron and ion conductivity, as well as good compatibility with other standard SOFC construction materials.[9] This combination of features may be useful in engineering low-temperature fuel cells with the performance necessary for more widespread application.

Since the surface structure and composition of real cathodes determine many of the performance attributes of fuel cells, investigations into cathode surface evolution give valuable insight towards improvement. Soft x-ray spectroscopy can provide element-specific chemical environment information for shallow sampling depths – precisely the region at play during operation. Previous x-ray studies have observed strontium segregation at the surface of LSCF films during operational-temperature annealing in air.[10] Similar effects have been observed in other strontium-based perovskite cathode materials.[11] The segregation of strontium and its oxides/carbonates at the surface has been shown[5,12] to decrease the sites available for oxygen catalysis as well as retarding electron transport to the surface, thereby negatively affecting the cell's long-term efficiency. It has also been shown that rapidly quenching the temperature of cathode films can preserve surface configuration changes, which allows for post-anneal or post-operation measurement.[10] However, exposure to atmospheric contaminants may interfere with surface-sensitive techniques, and surface treatment (e.g. degassing and cleaning) is necessary[13] for conventional soft x-ray measurements. To that end, a study of the low-temperature surface evolution is of interest for future surface studies that may require pristine films.

We report here the use of soft x-ray photoemission spectroscopy to determine the evolving chemical states on the surface of an LSCF film. Using very low (~10^{-8} torr) partial pressures, we demonstrate that existing surface carbon can be removed from the surface via annealing in argon. This technique produces a clean, defect-free film. Using similar pressures of oxygen during anneal cycles has drastically different results, incorporating surface carbon and bringing on a relatively strong insulating surface phase transition.

II. Methods

Pulsed laser deposition was used to grow epitaxial films of LSCF-6428 on $NdGaO_3$ substrates. The films were deposited using a LSCF target, at an oxygen partial pressure of 10 mTorr with the substrate temperature at 550°C. Films of approximately 250nm thickness were produced.

Soft x-ray spectroscopy measurements were performed at the soft x-ray undulator beamline X1B at the National Synchrotron Light Source, Brookhaven National Laboratory. Ultra-high vacuum (<10^{-9} torr) was maintained in the experimental chamber during data acquisition. X-ray photoemission spectroscopy (XPS) was performed using a hemispherical analyzer and monochromated incident x-rays at 250 and 900 eV. The total resolution of these spectra is approximately 0.4 eV full-width at half-maximum (FWHM) at the Sr 3*d* edge, and 0.7 eV FWHM at the oxygen and carbon *K*-edges. Binding energies were calibrated with reference to the 4*f* core levels of clean gold foil in electrical contact with the sample. In order to probe the surface chemistry of these materials, the soft x-rays employed are primarily surface-sensitive, and by varying the relative angle between the film surface and the photoelectron spectrometer, it is possible to tune the depth sensitivity for photoelectron spectroscopy. This has been used here to differentiate between surface and bulk chemical species.

After sonication in acetone, samples were mounted on tantalum foil, with the film grounded by tantalum strips. Samples were radiatively heated through the substrate using a bare tungsten filament. The power supplied to the filament was monitored using a constant voltage/current power supply. Temperatures reached on the sample surface were calibrated with a K-type thermocouple in contact with the surface.

Precautions were taken to ensure that chromium contamination, originating from the K-type thermocouple alloy, did not affect the films. The calibration was completed after XPS data were taken for all anneals, in order to avoid the thermocouple (TC) affecting the surface. While chromium poisoning is a well-known vulnerability of LSCF[8,15,16], it is worth noting that no chromium features were observed in XPS survey scans taken after the TC-contact calibrations. This suggests that chromium poisoning is not a concern at the temperatures used here, which is in reasonable agreement with thermodynamic calculations

performed[15] for other perovskites. Contact thermocouple temperature measurement may be utilized in this regime without negative consequence.

High-purity oxygen and argon were selectively dosed through a constant pressure valve (10^{-8} torr) with continuous pumping in the chamber, creating a steady supply of fresh gas across the sample surface. Oxygen was chosen for its role in the operational environment of SOFCs, and argon in order to provide contrast as an inert gas at the same partial pressures. For each anneal cycle, dosing and heating were combined for a period of time resulting in 50 Langmuir of total exposure. The samples were then quenched via abrupt power cutoff to the filament, and allowed to cool to room temperature in their respective annealing gases. The preparation chamber was then evacuated, and the film moved into a measurement chamber maintained at 10^{-10} torr.

III. Carbon 1*s*

Once a film has been exposed to air, it is subject to a number of contaminating adsorbents. For the present system the most notable contaminant is carbon in the form of atmospheric carbon dioxide; carbonates will tend to form[14] on surface strontium and its oxides. Since the experimental chamber is maintained under ultra-high vacuum (UHV), surface carbon carried in by the film can become a prime source of carbonate formation in addition to unavoidable carbon species already present in the chamber. An excess of surface carbon and its derivatives could potentially modify the surface chemistry in ways unrepresentative of the operating conditions we seek to mimic; it is therefore worthwhile to monitor the evolution of signal from carbon as the experiment proceeds.

The extent of carbon contamination on the surface can be directly studied through measurement of the carbon 1*s* core level. The relative height of the C 1*s* XPS peak near 285 eV compared to the strontium 3*p* peaks near 268 eV and 278 eV gives a good indication of how much carbon is adsorbed on the surface, since no carbon should be included in the bulk LSCF film. Figure 1 shows the core-level scans in the region of C 1*s*, for successive anneals in oxygen and argon at 10^{-8} torr.

A. Argon Atmosphere Annealing

Figure 1(a) shows the photoemission spectra taken after each annealing temperature for anneals in an argon partial pressure. The spectra show the C 1*s* peak at binding energy of 284.6 eV (with dotted line as a guide to the eye), as well as the strontium 3*p* doublet at 268.4 eV and 278.7 eV. It is clear that as the annealing temperature increases, the intensity of the C 1*s* peak reduces in intensity. This suggests that

the contaminant carbon desorbs from the surface as the temperature is increased, most significantly above 150 °C. Above 200 °C, contaminant carbon on the surface is below our detection limit.

Above 245 °C, an additional species develops on the sample surface, present as a doublet-like structure at 294-296 eV. After ruling out other contaminant elements, we identify this structure with chemically shifted carbon. This suggests the formation of new species as a result of carbon re-adsorption on the surface. The lack of strontium carbonate features (see section V) suggests that carbon is bonding to other elements present in the sample; in the current data set, the precise bonding environment of the re-adsorbed carbon species cannot be fully determined.

In summary, annealing LSCF in low partial pressure argon provides a route for a carbon-free surface, up to a certain temperature. The formation of carbonate species from ambient carbon cannot be avoided over 245 °C at these pressures in argon.

B. Oxygen Atmosphere Annealing

From Fig. 1(b) it can be seen that with increasing annealing temperature in oxygen there is a prominent reduction in the intensity of the C 1*s* peak, but not to the degree shown during argon anneals. In a pure oxygen atmosphere, a small fraction of surface carbon continues to persist throughout the anneal cycles. This is in addition to the re-adsorbed carbonate doublet, similar to that observed in argon anneals, which forms at higher temperatures for oxygen anneals (< 260 °C).

Even at very low partial pressures, an ambient oxygen atmosphere inhibits the removal of contaminant carbon from pristine LSCF film surfaces. For future surface studies that require clean LSCF, this result is of great practical use.

IV. Oxygen 1*s*

A. Argon Atmosphere Annealing

Since the operative function of a SOFC cathode is to reduce oxygen and move it into an electrolyte, observing the evolution of surface oxygen states is of primary interest in this investigation. Oxygen vacancies can be inferred and quantified from O 1*s* core level fitting.[17,18] Figure 2 shows the results obtained for the argon-annealed film. Figure 2(a) displays the O 1*s* spectrum for each successive anneal, where the temperature is increased from 98 °C to 290 °C. It is apparent that the O 1*s* spectra show prominent changes with increase in anneal temperature. We performed multi-peak fitting on the spectra, the results of which are shown in the right side panel. Figures 2(b), (c) and (d) respectively illustrate representative fits at room temperature, and at annealing temperatures of 220 °C and 278 °C.

For the multi-peak fitting applied here, a Shirley background is first subtracted from the spectrum and a Voigt line shape is used for each component. The O 1*s* spectra from pristine sample can be fitted with two components at binding energies of 528.5 eV and 531.5 eV. Varying the orientation of the film surface relative to the XPS spectrometer allows for selective depth profiling, from which it can be shown that the component at low binding energy originates from the bulk and the higher binding component is from surface layers. The two components will be respectively denoted as bulk and surface components for further discussion. At higher annealing temperatures a further component appears and the fitting of the spectra requires three components as shown in Figs. 2(b) and (c). The angle-dependent measurements show that this species is uniformly distributed in the surface and the bulk. Since it only arises during heating, and increases nearly linearly with temperature, it is likely the result of oxygen defects (vacancies) resulting from heating in an inert atmosphere.

To extract the evolution of each component of the O 1*s* core level spectra as the annealing temperature is increased, it is useful to examine the fractional area (individual area/total area) of each component during the experiment; these results are plotted in Fig. 3. Up to ~ 150 ^{o}C each curve in Fig. 3 shows a plateau, indicating that the area of each component remains unchanged even with increases in annealing temperature, and suggesting that the relative concentrations of oxygen species do the same. Above this temperature the component corresponding to vacancies increases almost linearly with temperature, showing the increase of defects in the material with increasing temperature. Above 150 ^{o}C there is a sharp rise in the area of the bulk component, which is accompanied by a sharp fall in the area of surface component. Between 150 ^{o}C and 175 ^{o}C there is an inversion of the surface:bulk character ratio. This can be correlated with observations at the strontium 3*d* edge (see section V), suggesting that the oxygen vacancies created through heating cause changes in the Sr-O bonding environment. Above 175 ^{o}C the area of the surface component increases approximately linearly and that of bulk component linearly decreases. Judging by these trends, the vacancies are forming at the expense of oxygen in the bulk. The surface oxygen, after a certain temperature has been reached, returns to its initial state and concentration.

B. Oxygen Atmosphere Annealing

The O 1*s* core levels are similarly followed during oxygen anneals. Figure 4(a) shows the O 1*s* core-level spectra for successive anneals in oxygen. In contrast to annealing in argon, the changes to the O 1*s* spectra are sudden and drastic for anneals in oxygen, as evidenced by the accompanying multi-peak fit. The representative fitting curves are shown in Figs. 4(b), (c) and (d) which respectively show spectra for pristine films, and films annealed at temperatures of 220 ^{o}C and 278 ^{o}C. As in the case of annealing in argon, the spectra can be fitted with 3 components: one bulk, one surface, and a third that only develops

upon heating in oxygen. It is important to note that this third species, induced by heating in a partial oxygen atmosphere, is not the same as the vacancy environment observed with argon anneals; it arises at an altogether different binding energy. The fractional area of each component is shown against the annealing temperature in Fig. 5.

Comparing Figs. 3 and 5 it can be seen that the there are prominent differences between the areas of different O 1*s* components depending on the annealing gas used. In oxygen (Fig. 5), as the temperature is increased, the area of the third species increases linearly and roughly saturates above 150 °C. This corresponds to the behavior one would expect of oxygen defect environments at low partial pressures; defects are formed in the surface and bulk, but eventually reach equilibrium with the replenishment provided by the ambient oxygen.

Thus the formation of vacancies is inhibited in the presence of oxygen at high temperatures, which is quite unlike the behavior during annealing in argon. Above 100 °C the bulk component decreases with temperature, which is accompanied by a corresponding increase in the surface component. The increasing surface-like character of the film may be a result of carbon incorporation (discussed above), the kinetics of which are clearly more favorable for a partial oxygen atmosphere, and carbonate formation, which still takes place at higher temperatures. The difference in "third" environment between inert gas (argon) and oxygen anneals can be accounted for by the incorporation of surface carbon; the environment indicative of an oxygen vacancy is altered by the persistent presence of carbon.

The stabilization of oxygen vacancies by low oxygen partial pressure was recently predicted theoretically by Luo *et al*.[19] Our results in both cases support that work, albeit at much lower pressures than discussed in Ref. 19.

V. Strontium

Strontium precipitation in its oxide and carbonate forms is widely accepted[5,20,21] to be one of the driving influences behind operational degradation of LSCF cathodes. Studies have shown conclusively that strontium precipitates are energetically favorable in these films when they are held in air (or other atmosphere-pressure gases) at high temperatures (> 600 °C) for long periods of time.

Figure 6 shows a typical Sr 3*d* core level. The 3*d* level is a doublet, with two peaks spaced 1.8eV apart due to the spin-orbit split $3d_{3/2}$ and $3d_{5/2}$ states.[22] Good agreement with the data is achieved by fitting this structure to a *pair* of Gaussian doublets and a linear background. In this fit, the energy separation and relative intensities of the doublet are fixed, and only the relative intensity between the two doublets and their energy separation is allowed to vary. Varying the relative orientation of the film's surface with respect to the spectrometer allows for relative depth profiling (as above), and in doing so the

lower binding energy doublet can be associated with the bulk, and the higher binding energy doublet is determined to originate at the surface.

Fitting the peaks to identify the surface and bulk phases allows for the observation of changes in the strontium concentration after anneal cycling. Figure 7 shows the fractional area of the bulk and surface components, plotted against the temperature at which the sample was annealed. At grazing incidence, these measurements are more surface sensitive; this is in good agreement with the fitted intensities for the bulk and surface components. Clear changes are visible throughout the heating process, as well as stark differences in the surface evolution between argon and oxygen anneals.

The integrated doublet areas are plotted as fractions of the total area of the fit in Fig. 7. Notably, the first points for the normal incidence behavior do not match, but they do for grazing incidence. This suggests that the surfaces for the respective samples are the same, but there is some difference in the bulk.

The above results can be explained by the specific geometry of the data acquisition chamber. The XPS collection aperture is 45° offset from the incoming x-rays. Rotating the sample increases the surface sensitivity due to the geometry of primary photoelectrons leaving the samples. Simultaneously the sampling area visible to the XPS aperture increases by a factor of $1/\cos(\theta)$. At grazing incidence for the data presented here, the sampling area is larger by over 30%. Local inhomogeneities in the film surface due to atmospheric contamination will therefore be more apparent at normal incidence, since the larger sampling area for grazing incidence will tend to average them out. This accounts for the difference in initial conditions present at normal incidence.

Certainly, prior to any heating at low pressure, the films can be expected to have slightly different surface contamination levels, in spite of identical cleaning and handling before insertion into UHV. After the film is gently annealed at 100 °C, but before surface carbon is strongly affected, the normal incidence bulk and surface areas are nearly the same. This supports the hypothesis that local differences in adsorbed atmospheric gases cause the initial difference.

Turning to the oxygen anneals (displayed by the solid lines in Fig. 7), it is worth noting that there are several distinct regions of change. For heating $\leq$ 100 °C, any visible change is likely due to the degassing of the film (visible in the carbon spectra presented above). Past the temperature at which carbon concentration begins to decrease at the surface, there is a clear trend of increase in the surface strontium concentration.

The argon anneal fractional areas (dotted lines) behave quite differently. Between the first and second heatings the bulk and surface phases behave in the opposite way to their oxygen-annealed counterparts. This is the interval during which the majority of carbon contamination is seen to leave the surface. Past the second anneal, the argon-annealed surface goes through an abrupt change in direction

and begins to develop towards the trend observed during the oxygen anneal. Notably, above 200 °C, argon annealing can return the strontium surface concentration close to its original configuration.

Eventually, near 300 °C, both types of annealed surfaces end up with nearly the same surface:bulk concentrations. Clearly not all of the carbon has been evacuated from the surface on the oxygen-annealed sample, as shown in the carbon core levels. Additionally, the oxygen-annealed sample goes through a phase transition to relatively strong insulating behavior (see Section VI), which is not visible in the argon-annealed sample. Both samples, notably, see an increase in surface-phase strontium concentration.

No contributions from $SrCO_3$ are seen in the strontium core levels. If carbonates form on the surface at these temperatures, they should[23] be visible as an additional doublet in the strontium spectra. The absence of such a feature suggests that strontium does not form its carbonate phase at these temperatures and pressures.

VI. Insulating Surface Phase

For both annealing gases employed in this study, we find that the films undergo a phase transition that promotes an insulating character at the surface near 300 °C. This insulating transition can be observed in time-resolved XPS scans, whereby the charging of the insulating surface develops with time and leads to large shifts in the apparent binding energies of core-level features. It is observed that argon-annealed films enter a "less insulating" state, even when annealed to higher temperatures.

Core level electrons from a conducting sample should have the same measured kinetic energy over time, assuming that the incident photon energy is constant and the originating core environment does not change. If the surface of a sample is gradually accumulating charge, the kinetic energy of a core level peak will shift in proportion to the total charge on the surface. Since electrons leave the surface, an overall positive charge will evolve in the sample, which in turn results in a net decrease in the kinetic energy of electrons emanating from the surface. Ultimately, this leads to an increase in the observed binding energy of core levels for samples that are not good conductors.

Figure 8 shows select time-resolved measurements of the Sr 3*d* core level for both samples. Fig. 8(a) shows the time-integrated intensity for a sample that does not exhibit charging. Fig. 8(b) shows a scan from a sample annealed in oxygen to 246 °C. Time proceeds from top to bottom, with each horizontal scan taking approximately 30 seconds. In the first color map, the horizontal (binding energy) position doesn't change appreciably with time. In Fig. 8(c), the binding energy of the peak clearly changes over time. This figure shows the same sample as in Fig. 8(b), but annealed to 260 °C in oxygen. The discrepancy in the location on the horizontal scales is due to the fact that the second scan was

acquired after the sample had already been exposed to the x-ray flux for some time, leading to a substantial accumulation in charge before the second measurement took place.

In contrast, Figs. 8(d) and (e) show the Sr 3*d* peaks of a sample annealed in argon at even higher temperatures. Above the point where the oxygen-annealed sample develops a surface insulating state that severely hampers the XPS measurements, the argon-annealed sample has no such transition. At higher temperatures the argon anneal appears to produce some insulating character, but not to the same severity that annealing in oxygen does. Below 300 °C, argon annealing mostly preserves the conducting character of the surface. Below 260 °C, the conducting character is entirely preserved.

VII. Conclusions

It has been shown that low temperature, low partial pressure treatment of LSCF films can be used to study oxygen environment evolution and strontium segregation at the surface of these films. Carbon contamination from atmospheric exposure can be selectively eliminated by annealing in an argon atmosphere or may be incorporated into the films using an anneal in oxygen. Carbonates of strontium are not observed, suggesting that temperatures in this regime are too low to provoke their large-scale formation. Oxygen vacancies are observed to plateau in number when the anneal takes place in low oxygen partial pressure, but increase linearly with temperature when argon is used. Annealing in argon at temperatures of 200-245 °C produces a clean, carbon-free surface with an added environment of surface and bulk oxygen vacancies.

Figure Captions

Figure 1: XPS spectra showing C 1*s* and Sr *3p* core levels after successive anneals in 10^{-8} torr partial pressure of (a) argon and (b) oxygen. Surface carbon appears in both near 285eV; a dotted line is provided as a guide to the eye.

Figure 2: Oxygen *1s* spectra (a) for argon-annealed films. Typical multi-peak fits are shown in (b-d). Fits were performed using Voigt peaks with a Shirley background.

Figure 3: O*1s* core level multi-peak Voigt fit fractional areas, argon-annealed film.

Figure 4: O1*s* core levels (a), oxygen annealed film. Multi-peak fits (b-d) performed using same technique as Fig.2.

Figure 5: O*1s* core level multi-peak Voigt fit fractional areas, oxygen-annealed film.

Figure 6: Typical strontium *3d* core level for LSCF-6428. Best fit for two Gaussian doublets with linear background plotted against data. Inset shows the determination of surface v. bulk states by angular surface sensitivity increase; as the surface angle with respect to the spectrometer increases, the measurement is more surface sensitive.

Figure 8: Fractional areas of the surface/bulk strontium phases over successive heating cycles, at (a) normal and (b) grazing incidence. Grazing incidence is more surface-sensitive.

Figure 9: Time-resolved scans of Sr*3d* core levels. Time per scan is approximately 45 seconds. From top to bottom: (a) A plot showing integrated intensity over time for a well-conducting sample. (b) A time-resolved scan of a film annealed in O_2 at 246°C, in which time proceeds down the y-axis.(c) A time-resolved scan clearly showing charge buildup over time after O_2 annealing at 260°C. (d),(e) Two more scans, of argon-annealed films annealed to over 278°C, showing little charge buildup.

References

1. EG&G Technical Services, DOE Fuel Cell Handbook,7th Edition (2004).

2. Singhal, S. Solid State Ionics, 135(1-4), 305–313 (2000).

3. G. Cinti, U. Desideri, D. Penchini, and G. Discepoli, Fuel Cells **14**, 221 (2014).

4. A.C. Rady, S. Giddey, A. Kulkarni, S.P.S. Badwal, S. Bhattacharya, and B.P. Ladewig, Appl. Energy **120**, 56 (2014).

5. D. Oh, D. Gostovic, and E.D. Wachsman, J. Mater. Res. **27**, 1992 (2012).

6. Weber, A., & Ivers-Tiffée, E. Journal of Power Sources, **127**(1-2), 273–283 (2004).

7. Singhal, S., & Kendall, K. (Eds.). Chemical Society Reviews. Elsevier (2003).

8. C. Sun, R. Hui, and J. Roller, J. Solid State Electrochem. **14**, 1125 (2009).

9. Baharuddin, N. A., Rahman, H. A., Muchtar, A., Sulong, A. B., & Abdullah, H. J. Zhejiang Univ. S cience A, 14(1), 11-24 (2013).

10. Davis, J. N., Miara, L. J., Saraf, L., Kaspar, T. C., Gopalan, S., Pal, U. B., Ludwig, K. F. ECS Transactions, 41(11), 19-24 (2012)

11. Monsen, Å. F., Song, F., Li, Z. S., Boschker, J. E., Tybell, T., Wahlström, E., & Wells, J. W. (2012). Surface Science, 606(17-18), 1360–1366. doi:10.1016/j.susc.2012.04.018

12. Y. Chen, W. Jung, Z. Cai, J.J. Kim, H.L. Tuller, and B. Yildiz, Energy Environ. Sci. **5**, 7979 (2012).

13. Piper, L. F. J., et al. Journal of The Electrochemical Society, 158(2), B99 (2011)

14. V. Young and T. Otagawa, Appl. Surf. Sci. **20**, (1985).

15. H. Yokokawa, T. Horita, N. Sakai, K. Yamaji, M. Brito, Y. Xiong, and H. Kishimoto, Solid State Ionics **177**, 3193 (2006).

16. S. Taniguchi, M. Kadowaki, H. Kawamura, T. Yasuo, Y. Akiyama, Y. Miyake, and T. Saitoh, J. Power Sources **55**, 73 (1995).

17. Butcher, K. S. a., Fernandes, a. J., Chen, P. P.-T., Wintrebert-Fouquet, M., Timmers, H., Shrestha, S. K., Usher, B. F. Journal of Applied Physics, 101(12) (2007).

18. Rumaiz, A. K., Ali, B., Ceylan, A., Boggs, M., Beebe, T., & Ismat Shah, S. Solid State Communications, 144(7-8), 334-338 (2007).

19. H. Luo, Y. Shin, Y. Yu, D. Cetin, and K. Ludwig, Pre-Print (Applied Surf. Sci.) (n.d.).

20. F. Wang, M.E. Brito, K. Yamaji, D.-H. Cho, M. Nishi, H. Kishimoto, T. Horita, and H. Yokokawa, Solid State Ionics **2** (2014).

21. E. Bucher and W. Sitte, Solid State Ionics **192**, 480 (2011).

22. G. Williams, X-RAY DATA Booklet. (2001).

23. P. a. W. van der Heide, Surf. Interface Anal. **33**, 414 (2002).

Figure 1

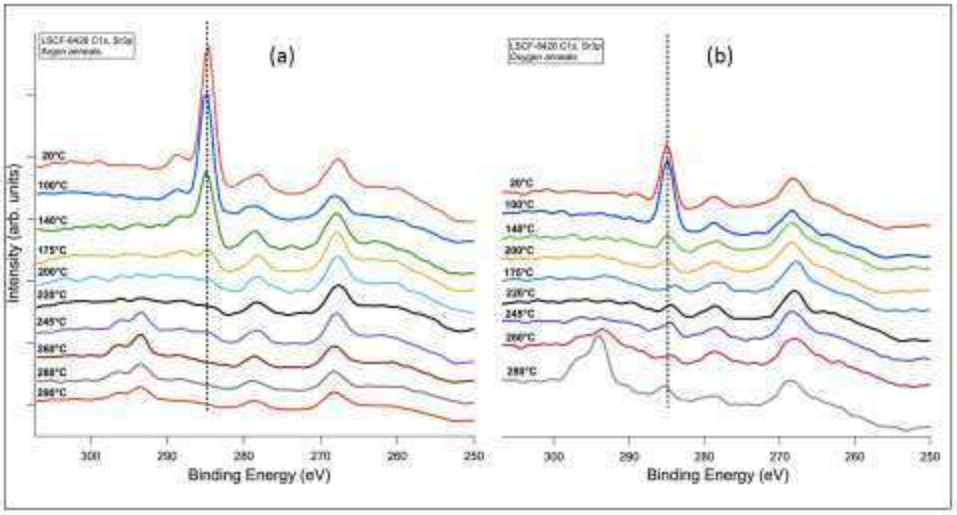

Figure 2

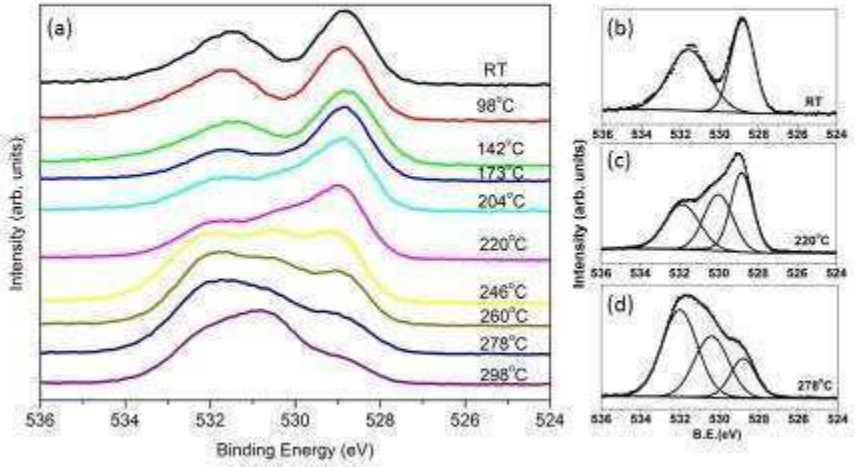

Figure 3

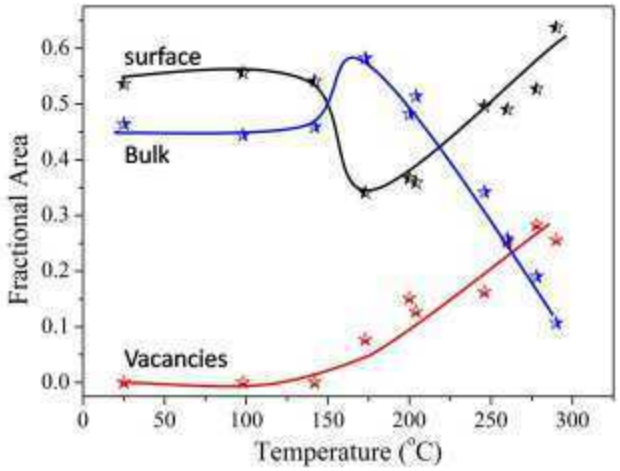

Figure 4

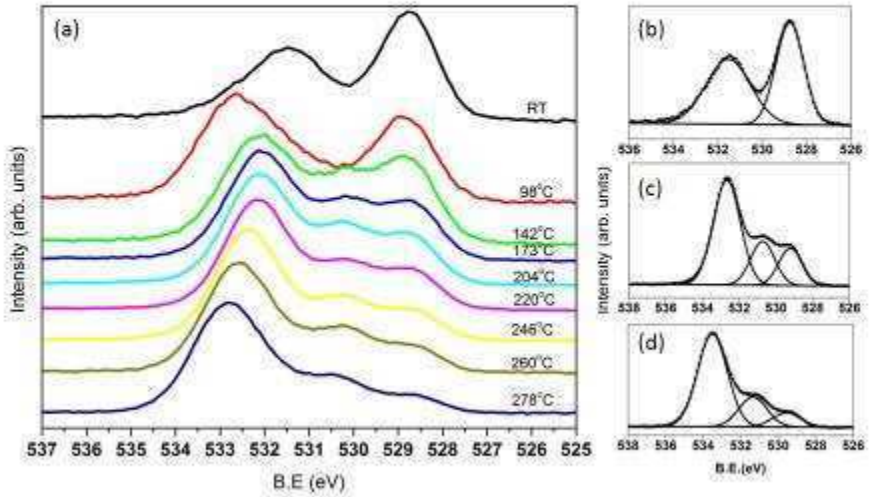

Figure 5

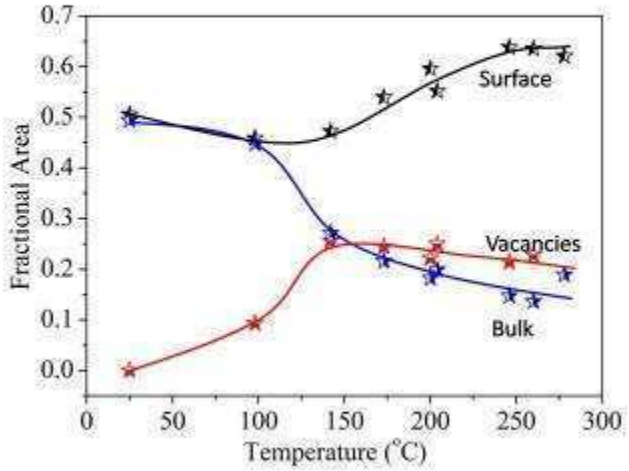

Figure 6

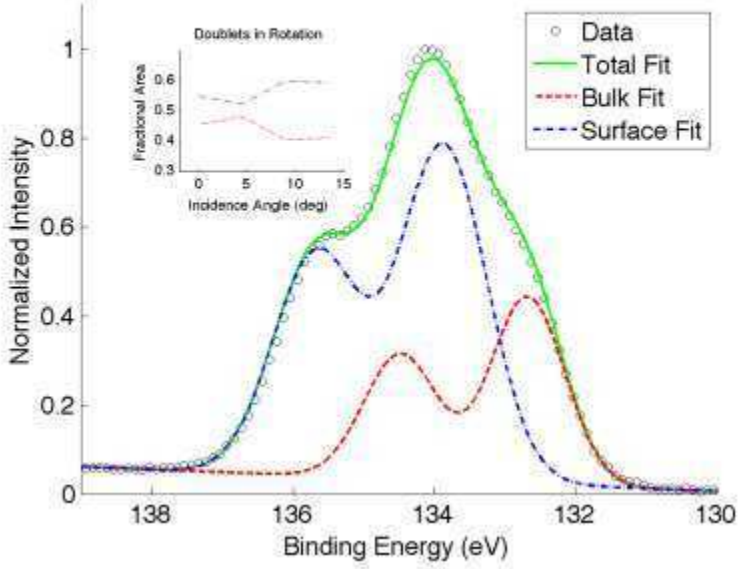

Figure 7

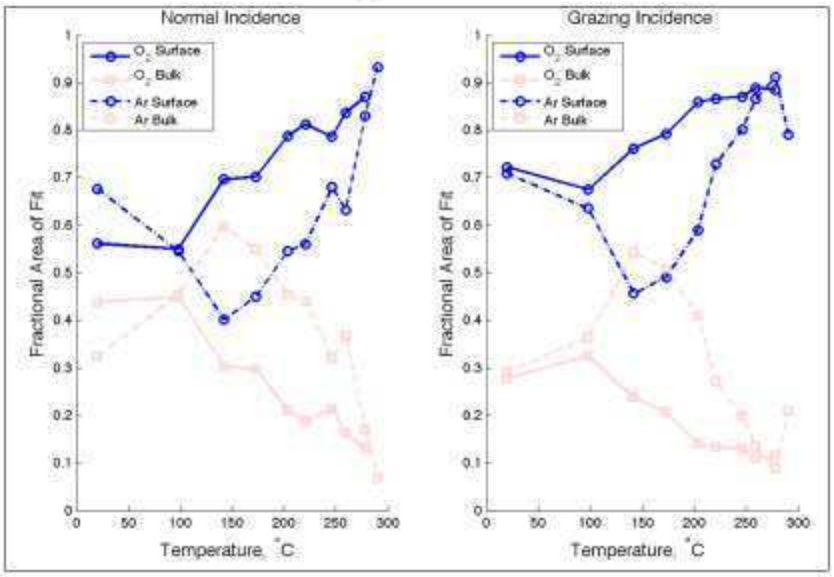

Figure 8

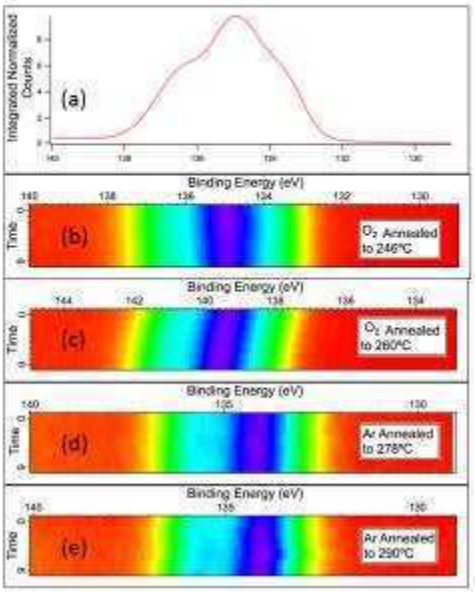

Reprinted from: D.Newby Jr, J.Kuyyalil, J.Laverock, K.F.Ludwig, Y.Yu, J.Davis, S.Gopalan, U.B.Pal, S.Basu, and K.E.Smith, "Surface evolution of lanthanum strontium cobalt ferrite thin films at low temperatures", *Thin Solid Films,* 589 (2015) 655-661with permission from Elsevier.

Thermodynamic Stabilities of $Ba_{0.5}Sr_{0.5}Co_{0.8}Fe_{0.2}O_{3-\delta}$, $Sr_2Fe_{1.5}Mo_{0.5}O_{6-\delta}$ and $La_{0.6}Sr_{0.4}Co_{0.2}Fe_{0.8}O_{3-\delta}$ Using Molten Salt Method

Deniz Cetin[1], Keping Hua[2], Zhangzhengrong Feng[2], and Srikanth Gopalan[1,2]

[1]Division of Materials Science and Engineering, Boston University, 15 Saint Mary's Street, Brookline 02446, USA
[2]Department of Mechanical Engineering, Boston University, 110 Cummington Mall, Boston 02215, USA

We have tested $Ba_{0.5}Sr_{0.5}Co_{0.8}Fe_{0.2}O_{3-\delta}$ (BSCF), $Sr_2Fe_{1.5}Mo_{0.5}O_{6-\delta}$ (SFM) and $La_{0.6}Sr_{0.4}Co_{0.2}Fe_{0.8}O_{3-\delta}$ (LSCF) are three, promising cathode materials for application in low temperature SOFC systems. In this work, their stability has been tested by equilibrating them in a eutectic molten salt mixture of LiCl-KCl in air. Both single-phase BSCF and SFM decomposed into their carbonate and oxide precursors in air, but LSCF retained its single phase. This study suggests that BSCF and SFM cathode materials are thermodynamically unstable with respect to their carbonate precursors in eutectic molten salts in air.

Introduction

$Ba_{0.5}Sr_{0.5}Co_{0.8}Fe_{0.2}O_{3-\delta}$ (BSCF), $Sr_2Fe_{1.5}Mo_{0.5}O_{6-\delta}$ (SFM) and $La_{0.6}Sr_{0.4}Co_{0.2}Fe_{0.8}O_{3-\delta}$ (LSCF) are promising cathode materials for solid oxide fuel cell (SOFC) systems operating at intermediate temperatures (600°C -800°C, (1-5)), due to their high electronic and ionic conductivity and facile oxygen exchange kinetics. Yet, recent studies (6-9) have suggested that BSCF and SFM may be thermodynamically unstable in the presence of carbon dioxide. Moreover, recent studies (10,11) show that LSCF exhibits cation surface segregation, which raises concerns about the bulk stability of the material. In this paper, we show that indeed BSCF and SFM are thermodynamically unstable with respect to their constituent oxide and carbonate precursors using a molten salt technique. By contrast, molten salt studies proves that LSCF is thermodynamically stable material with respect to its oxide and carbonate precursors in air.

Compared to transport in solid state, transport in molten salts is higher by many orders of magnitude. For instance, bulk diffusivity of Fe in $LaFeO_3$ at 1200°C is of the magnitude of 10^{-12} m^2/s (12), whereas in molten salts typical cation-anion diffusivities are about 10^{-9} m^2/s range (13). Therefore, kinetics of chemical reactions in molten salts are also expected to be much faster even at low temperatures, than solid state reactions at high temperatures. In that sense, decomposition reactions should also be rapid to allow the determination of the thermodynamic stability of cathode materials at low temperatures.

The molten salt method has been sporadically used for the low temperature synthesis of a large number of perovskite and other types of ternary oxide materials (14-22). Due to the low synthesis temperature afforded by the molten salt method, control of particle size and morphology has been (18-23) made possible. Besides perovskites, synthesis of materials like $BaFe_{12}O_{19}$ and $SrFe_{12}O_{19}$ (23), NiZn-ferrite (24), and $PbNb_2O_6$

(25) has been demonstrated. Additionally, this method has been used to study phase stability and phase equilibria of materials (16, 26-28). For instance, Gopalan and Virkar (28) showed the thermodynamic instability of $BaCeO_3$ and $SrCeO_3$ in both NaOH-KOH and LiCl-KCl eutectics in the temperature range of 390-550^oC both in air and in essentially CO_2-free air. $SrCeO_3$ was reported to decompose into $SrCO_3$ and CeO_2 (in air) and into SrO and CeO_2 (upon removal of CO_2 from air). Decomposition products of $BaCeO_3$ were $BaCO_3$ and CeO_2 in both presence and absence of CO_2. Moreover, Naidu and Virkar (27) used the LiCl-KCl eutectic to determine the phase diagram of TiO_2-SnO_2 down to 400°C, which might be too slow to study through solid state annealing method due to about 10 orders of magnitude difference in cation andanion diffusivities in solid state diffusion versus diffusion through the molten salt.

As stated by Meng and Virkar, there are two requirements for testing the stability of materials in molten salt: 1) the initial precursors and the final product should not react with the molten salt system –selection of inert molten salt system is important; 2) all dissolved components should have uniform and low solubility in the molten salt. The expected route for the process includes dissolution and diffusion of constituents in molten salt, reaction of the constituents with dissolved gases and ionic phases in molten salt, and precipitation of the final compounds out of the molten phase upon exceeding the solubility limit (28).

The main objective of this paper is to investigate the thermodynamic stability of the BSCF and SFM under molten salt conditions. Eutectic mixture of LiCl-KCl is utilized in this study. The thermodynamic stabilities of BSCF and SFM are tested by adding single-phase cathode powders synthesized by high temperature calcination, into the molten salt media and analyzing the resulting products by X-ray diffraction (XRD).

Experimental

The single-phase BSCF, LSCF and SFM were prepared by solid state synthesis in air. Their constituent precursors (namely; $BaCO_3$, $SrCO_3$, Co_3O_4, Fe_2O_3 for BSCF and $SrCO_3$, Fe_2O_3, MoO_3 for SFM) were mixed in stoichiometric ratios in ethanol and ball-milled for 24 hours in zirconia ball media. After evaporating the ethanol, the mixed precursors were calcined in air at 1150°C for 4 hours for BSCF and SFM, at 1200°C for 4 hours for LSCF. Single phase formation was confirmed by X-ray diffraction.

The molten salt mixtures were prepared by using a eutectic composition of KCl (41 mol%) –LiCl (59 mol%) at Teu= 355°C. The salt to ceramic powder ratio was held at 5:1 by weight and the powders were added into the salts, once melting had occurred. The temperature of the set up was maintained at least 40°C higher than the eutectic melting temperature of the salts. The mixture was occasionally stirred and the mixture was maintained at temperature for about 5h. After cooling the set-up and freezing the salt, the salt-powder mixtures were washed multiple times with distilled water to dissolve the salt away. After completely drying the residue in a drying oven at 70°C, X-ray diffraction patterns were obtained using Cu-Kα radiation.

Results

The X-ray diffraction patterns before and after the molten salt experiment of BSCF is presented in Figure 1. Figure 1a shows single phase cubic BSCF obtained by solid state reaction at 1150^{o}C. Figure 1b shows the products of reaction in the molten salt medium, namely, a solid solution of barium carbonate and strontium carbonate that can be fitted to an orthorhombic structure. The presence of alkaline earth carbonates is very clear in the resulting XRD pattern after exposure to molten salts. The other phases present as can be seen in Fig. 1b have been indexed to hexagonal-CoO and cubic-Fe_2O_3, however since they can form structures with multiple ionic charge states present, it is possible that other transition metal oxide structures including spinels have formed in the product. Nonetheless, it is clear that the XRD pattern after molten salt exposure indicates that BSCF has decomposed into alkaline earth carbonates and transition metal oxides.

Figure 2 shows the XRD pattern of single phase cubic SFM synthesized by solid state reaction and after its exposure to molten salt. The resulting powder after equilibration in the molten salt clearly shows the orthorhombic strontium carbonate peaks.

XRD patterns of LSCF before and after molten salt exposure are shown in Figure 3. The peaks of the perovskite LSCF have been indexed as cubic phase before the molten salt experiment. No degradation or phase change of LSCF has been observed upon its exposure to molten salt environment.

Discussion

Decomposition of the single phase BSCF and SFM powders into their constituent carbonates and oxides indicates the thermodynamic instability of these cathode powders with respect to their constituent carbonates and oxides in the molten salt environment. Instability of these cathode materials at temperatures as low as 400°C, the operating temperature for these experiments, suggest that these materials are not suitable for long-term application in fuel cell stacks. Unforeseen shut downs during stack operations may cause the cathode material to decompose and therefore destroy the cathode microstructure. Specifically, the materials are not stable against carbonate formation even in the trace amounts of carbon dioxide (400 ppm) present in ambient air. High carbon dioxide concentrations in the air stream, possibly due to leaks from the anode side, might cause degradation of the cathode material, which is detrimental to the SOFC operation in long terms.

On the other hand, LSCF remained single phase upon exposure to molten salt media, which suggests the thermodynamic stability of LSCF as a bulk cathode material in air. Even though previous studies indicate Sr cation segregation on the LSCF surfaces, through this molten salt work we suggest that LSCF is a stable bulk material.

Conclusion

BSCF and SFM are unstable in air in molten salt conditions with respect to their constituent precursors. This study suggest unsuitability of these cathode materials for SOFC applications. By contrast, LSCF remains stable in air.

References

1. Shao, Z., & Haile, S. M. Nature, 431 (7005), 170-173 (2004).
2. Bucher, E., Egger, A., Ried, P., Sitte, W., & Holtappels, P. Solid State Ionics, 179(21), 1032-1035 (2008).
3. Zhang, L., Liu, Y., Zhang, Y., Xiao, G., Chen, F., & Xia, C. Electrochemistry Communications, 13(7), 711-713 (2011).
4. Liu, Q., Yang, C., Dong, X., & Chen, F. International Journal of Hydrogen Energy, 35(19), 10039-10044 (2010).
5. S. Wang, M. Katsuki, M. Dokiya and T. Hashimoto, Solid State Ionics, 2002, 152–153, 777.
6. Švarcová, S., Wiik, K., Tolchard, J., Bouwmeester, H. J., & Grande, T. Solid State Ionics, 178(35), 1787-1791 (2008).
7. Niedrig, C., Taufall, S., Burriel, M., Menesklou, W., Wagner, S. F., Baumann, S., & Ivers-Tiffée, E. Solid State Ionics, 197(1), 25-31 (2011).
8. Yan, A., Liu, B., Dong, Y., Tian, Z., Wang, D., & Cheng, M. Applied Catalysis B: Environmental, 80(1), 24-31 (2008).
9. Yan, A., Maragou, V., Arico, A., Cheng, M., & Tsiakaras, P. Applied Catalysis B: Environmental, 76 (3), 320-327(2007).
10. W. Jung and H. L. Tuller, Energy Environ. Sci. (5) 5370 (2012)
11. Ding, H., Virkar, A. V., Liu, M., Liu, F., Phys. Chem. Chem. Phys., (15), 489, (2013).
12. V. V. Kharton, Solid state electrochemistry II: electrodes, interfaces and ceramic membranes, p. 435, Wiley-VCH, Weinheim, (2011).
13. G. J. Janz, Molten Salt Handbook; pp. 334 and 39. Academic press, New York, 1967.
14. Gopalan, S., Mehta, K., & Virkar, A. V. Journal of materials research, 11 (08), 1863-1865(1996).
15. Arendt, R. H., Rosolowski, J. H., & Szymaszek, J. W. Materials Research Bulletin, 14(5), 703-709 (1979).
16. Meng, W., & Virkar, A. V. Journal of Solid State Chemistry, 148(2), 492-498 (1999).
17. Thirumal, M., Jain, P., & Ganguli, A. K. Materials chemistry and physics, 70(1), 7-11 (2001).
18. Yoon, K. H., Cho, Y. S., Lee, D. H., & Kang, D. H. Journal of the American Ceramic Society, 76(5), 1373-1376 (1993).
19. Chiu, C. C., Li, C. C., & Desu, S. B. Journal of the American Ceramic Society, 74 (1), 38-41(1991).
20. Zhou, H., Mao, Y., & Wong, S. S. Chemistry of Materials, 19(22), 5238-5249 (2007).
21. Li, H. L., Du, Z. N., Wang, G. L., & Zhang, Y. C. Materials Letters, 64(3), 431-434 (2010).
22. Zeng, J. T., Kwok, K. W., & Chan, H. L. W. Materials Letters, 61(2), 409-411 (2007).

23. Arendt, R. H. Journal of Solid State Chemistry, 8(4), 339-347 (1973).
24. Hayashi, Y., Kimura, T., & Yamaguchi, T. Journal of materials science, 21 (8), 2876-2880 (1986).
25. Granahan, M., Holmes, M., Schulze, W. A., & Newnham, R. E. Journal of the American Ceramic Society, 64(4), c-68 (1981).
26. Kimura, T., Kanazawa, T., & Yamaguchi, T. Journal of the American Ceramic Society, 66(8), 597-600 (1983).
27. Naidu, H. P., & Virkar, A. V. Journal of the American Ceramic Society, 81(8), 2176-2180 (1998).
28. Gopalan, S., & Virkar, A. V. Journal of the Electrochemical Society, 140(4), 1060-1065 (1993).

List of Figures

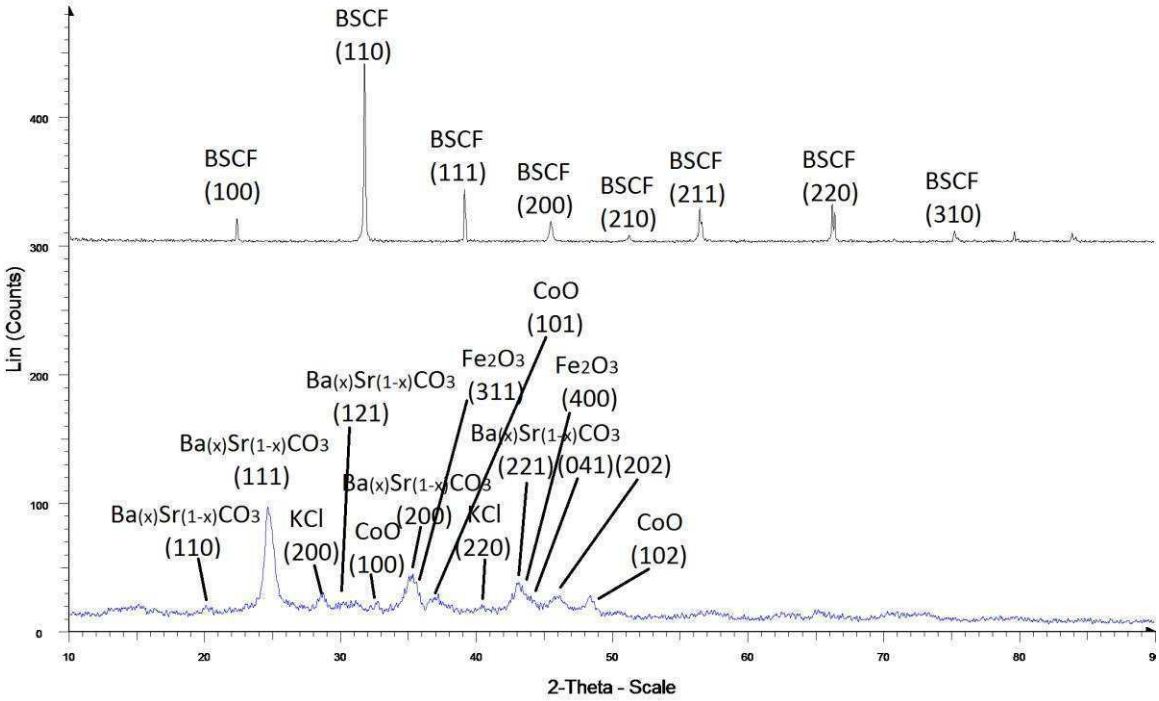

Figure 1

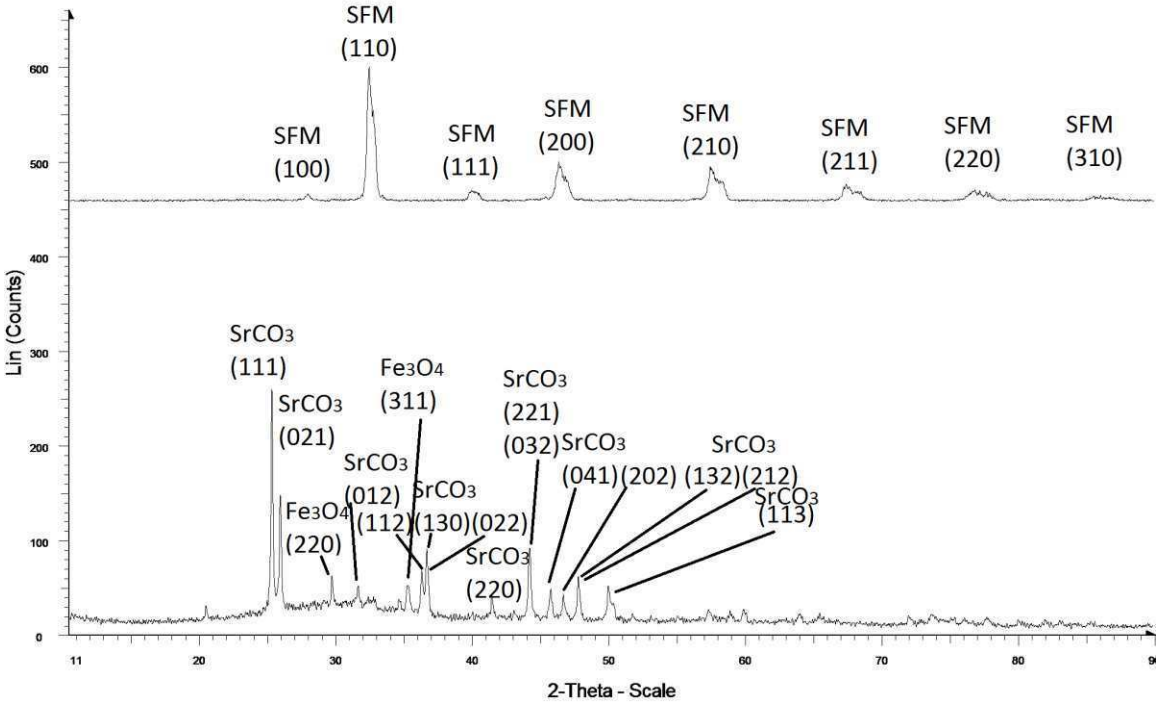

Figure 2

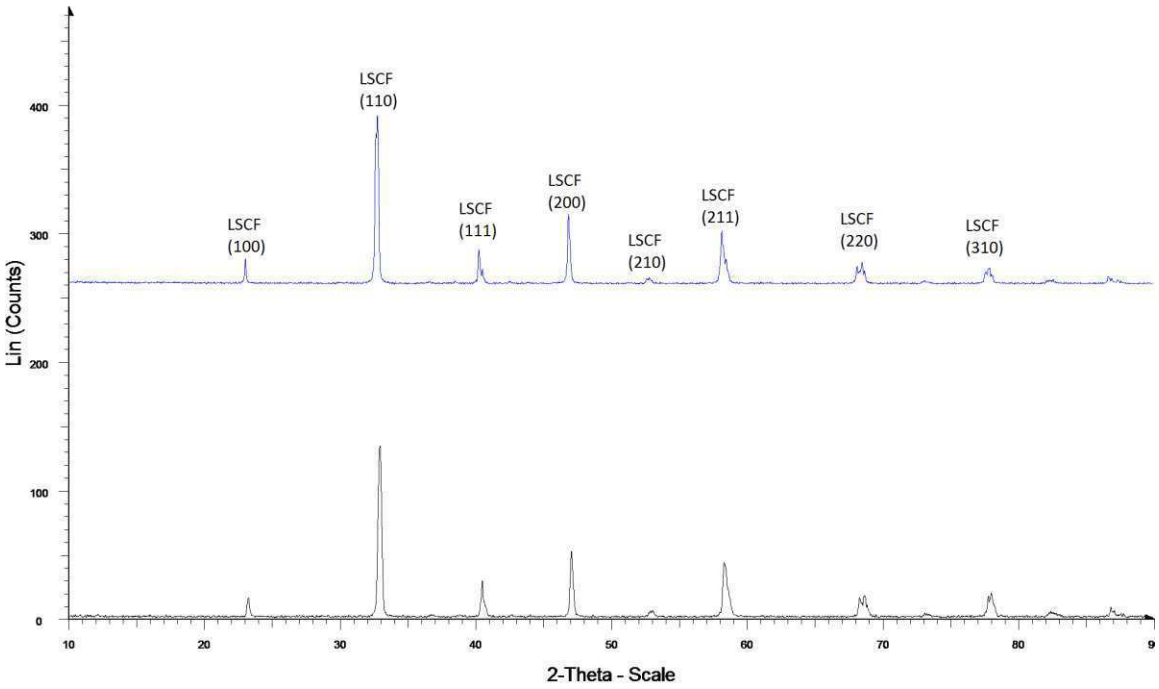
LSCF
(110)
LSCF
(100)
LSCF
(111)
LSCF
(200)
LSCF
(210)
LSCF
(211)
LSCF
(220)
LSCF
(310)
Lin (Counts)
2-Theta - Scale

Figure 3